Hallmarks of Optimization Trajectories in Neural Networks and LLMs: The Lengths, Bends, and Dead Ends

Sidak Pal Singh [1 2] **Bobby He** [1] **Thomas Hofmann** [1] **Bernhard Schölkopf** [1 2]

Abstract

We propose a fresh take on understanding the mechanisms of neural networks by analyzing the rich structure of parameters contained within their optimization trajectories. Towards this end, we introduce some natural notions of the complexity of optimization trajectories, both qualitative and quantitative, which reveal the inherent nuance and interplay involved between various optimization choices, such as momentum, weight decay, and batch size. We use them to provide key hallmarks about the nature of optimization in deep neural networks: when it goes right, and when it finds itself in a dead end. Further, thanks to our trajectory perspective, we uncover an intertwined behaviour of momentum and weight decay that promotes directional exploration, as well as a directional regularization behaviour of some others. We perform experiments over large-scale vision and language settings, including large language models (LLMs) with up to 12 billion parameters, to demonstrate the value of our approach.

1. Introduction

Given a network architecture and the training task, the loss landscape — which is the high-dimensional surface whose each point characterizes the fit of the parameters to the task objective — entails the possible trajectories that might be followed by an optimization algorithm, such as stochastic gradient descent (SGD). The particular sets of paths are determined, to no less extent, by the particular optimization choices and hyperparameters, such as the learning rate, momentum, batch size, weight decay, and more. We might even say that the regions and topographical features of the landscape that are never encountered or realized in typical optimization paths, might as well not be in the landscape. *Essentially*, the optimization trajectories are the probes through which the loss landscape is accessed.

Consequently, a significant body of literature builds around the principle of an inherently regular manner of traversing in the landscape, i.e., the implicit bias (Gunasekar et al., 2018; Li et al., 2019; 2020; Moroshko et al., 2020), facilitated by optimization algorithms. This preferential landscape access is in comparison with the actual surface level, possibly treacherous, non-convexity, and thus suggesting that the network stays clear of sub-optimal local minima. Therefore, despite the complexity of the neural landscapes, implicit bias lends a formal and reasonable support to the empirical success of massively over-parameterized neural networks

If that is indeed the case, we might expect to see traits and hallmarks of regularity in the sequence of steps that make up the optimization trajectories of neural networks in the loss landscape. In other words, it raises the following questions,

> *How are these trajectories structured? Are these paths long or short, with zigzags or soft bends, reaching the solution winding and coiling or straight and direct? What, if at all, do they reveal about the generalization strategy?*

This, in essence, is the key research theme of our study here. More precisely, we explore and develop key qualitative as well as quantitative indicators (hallmarks) about the complexity/regularity of the optimization trajectory. In particular, towards this end, we analyze and compare multiple intermediate checkpoints amongst themselves, across different scenarios and large-scale case studies. The qualitative hallmark, which we call the *'Trajectory Map'*, conveys the directional (dis)similarity of the parameters and visually depicts the nature of optimization within and across various stages of training, i.e. at a pan-trajectory level. The quantitative hallmarks are functions of these trajectory maps, that measure various notions of lengths and angles, over and about the sequence of steps in the trajectory.

We form it as a focus of our investigation to study the properties of trajectories and their ensuing implications about the nature of found solutions since it, (a) brings in a level of architecture agnosticity and helps unlock shared insights onto features of optimization, (b) contains an intrinsic data-

[1]ETH Zürich, Switzerland [2]MPI for Intelligent Systems, Tübingen. Correspondence to: Sidak Pal Singh <sidak.singh@inf.ethz.ch>.

dependence that, for all intents and purposes, implies no explicit inference over additional data samples is needed (which anyway might not be possible due to resource or privacy constraints), (c) allows analyzing and prognosing the developing generalization strategy on-the-fly, over the course of training (instead of waiting all the way until convergence to assess the solution quality), and (d) provides potential hints at the bottlenecks and redundancies plaguing the optimization procedure.

Hence, given these factors, we naturally do not expect the above trajectory viewpoint to cover and uncover all aspects of the desired phenomenology at stake, but we hope to at least offer an outlook into the concerned phenomenon based on the corresponding optimization trajectories (and their directional complexity), such as when considering the implicit effects of momentum and weight decay, and thus provide novel insights into the inner-workings of neural networks and their optimization.

2. Methodology

Matrix representation of Trajectory. Let us assume the optimization trajectory consists of a set $\mathcal{T}$ of points $\{\boldsymbol{\theta}_t\}_{t=0}^{T}$, each denoting the (flattened) parameters of the network encountered at some step and which live in the parameter space $\Theta = \mathbb{R}^p$, i.e., $\mathcal{T} \subseteq \Theta$. This set of points need not contain the entire set of points visited in the course of optimization but instead can represent a subset of points, possibly sampled at an interval of k points.[1] It will be convenient to organize this set of points which define the trajectory in the form of a matrix, $\boldsymbol{\Theta} \in \mathbb{R}^{(T+1)\times p}$, whose first dimension $T+1$ makes explicit the inclusion of the initialization $\boldsymbol{\theta}_0$.

Elsewhere it will be useful to analyze the trajectory relative to some point $\boldsymbol{\theta}_\tau$ as the origin, i.e., we will instead consider the set of points $\mathcal{T}_\tau = \{\boldsymbol{\theta}_t - \boldsymbol{\theta}_\tau\}_{t=0}^{T}$, and correspondingly organize it in the matrix $\boldsymbol{\Theta}_\tau \in \mathbb{R}^{(T+1)\times p}$. When τ is itself one of the points of the trajectory, then we will omit the row of zeros and shape the matrix of size $\mathbb{R}^{T\times p}$. A natural point from where to view the trajectory would be the initialization $\boldsymbol{\theta}_0$, and this relative trajectory will then be denoted as $\boldsymbol{\Theta}_0$ (where the subscript 0 is not to be confused for the usual origin O, namely, $\boldsymbol{\theta}_O = \mathbf{0}$).

Trajectory Map. Analyzing the matrix $\boldsymbol{\Theta}$ or $\boldsymbol{\Theta}_\tau$, on its own, might get cumbersome as the size of modern networks ranges in millions and billions of parameters. Hence, we will resort to looking at functions of the kernel matrix $\mathbf{K} = \boldsymbol{\Theta}\boldsymbol{\Theta}^\top$ which would be a square matrix of shape $n = T+1$, or for $\tau \neq O$, the relative kernel matrix $\mathbf{K}_\tau = \boldsymbol{\Theta}_\tau\boldsymbol{\Theta}_\tau^\top$ of shape $n = T+1$ or $n = T$ depending if the point $\boldsymbol{\theta}_\tau$ is a part of the trajectory or not. Further, it will also be helpful to isolate and analyze the directional aspect of the trajectory, for which we will normalize the set of points by their norm, and in effect, consider the set $\widehat{\mathcal{T}}_\tau = \{\frac{\boldsymbol{\theta}_t - \boldsymbol{\theta}_\tau}{\|\boldsymbol{\theta}_t - \boldsymbol{\theta}_\tau\|_2}\}_{t=0}^{T}$ with the respective matrix $\widehat{\boldsymbol{\Theta}}_\tau$. As a result, the ensuing kernel matrix $\widehat{\boldsymbol{\Theta}}_\tau\widehat{\boldsymbol{\Theta}}_\tau^\top$, which we will refer to as $\mathbf{C}_\tau$ (or $\mathbf{C} := \mathbf{C}_O$ for the usual origin $\tau = O$), will contain the relative cosine similarities between every pair of points in the trajectory. So, $(\mathbf{C}_\tau)_{ij}$ is,

$$\text{cos-sim}(\boldsymbol{\theta}_i - \boldsymbol{\theta}_\tau, \boldsymbol{\theta}_j - \boldsymbol{\theta}_\tau) = \frac{\langle \boldsymbol{\theta}_i - \boldsymbol{\theta}_\tau, \boldsymbol{\theta}_j - \boldsymbol{\theta}_\tau \rangle}{\|\boldsymbol{\theta}_i - \boldsymbol{\theta}_\tau\|_2 \, \|\boldsymbol{\theta}_j - \boldsymbol{\theta}_\tau\|_2} \,.$$

Hereafter, we will refer to $\mathbf{C}$ as the *Trajectory Map* (TM) and $\mathbf{C}_\tau$ (for $\tau \neq O$) as the *Relative Trajectory Map* (RTM). We would like to remark that, although not necessary, here we are essentially considering linear kernels, for as we will see they deliver a great mileage by themselves. The TM will be our qualitative hallmark of choice for analyzing optimization trajectories.

Quantitative Hallmarks. Besides visualizing the TM as the qualitative hallmark, we will consider the following set of indicators for quantitatively hallmarking the optimization trajectories.

(i) Mean Directional Similarity (MDS): We take the cosine similarity averaged over the entire trajectory map, i.e., over every pair of points in the trajectory. This can be written as, $\omega := \frac{1}{n^2}\, \mathbb{1}_n^\top \cdot \mathbf{C} \cdot \mathbb{1}_n$, where $\mathbb{1}_n^\top = (1 \cdots 1)^\top \in \mathbb{R}^{1\times n}$ denotes the vector of all ones and $n = |\mathcal{T}|$ is the cardinality of the trajectory. By using the form of the matrix $\mathbf{C}$ discussed before, we can further rewrite MDS as, $\omega = \left\| \frac{1}{n}\, \widehat{\boldsymbol{\Theta}}^\top \mathbb{1}_n \right\|^2$. Now, it becomes apparent that MDS essentially projects all the trajectory points onto the unit sphere, computes their average and finally takes the squared norm.

To get a better sense of MDS, we can consider its two possible extremes: (a) all the parameter unit-vectors cancel out, yielding a value of $\omega = 0$. For instance, this would happen in the scenario when the points in the trajectory are exactly following a circular orbit around the origin; or, (b) when each of the parameters point in the same direction, implying that the trajectory is simply a linear path, with $\omega = 1$. Knowing the nature of these two extremes, we can expect neither of them to be desirable in an ideal trajectory which leads up to a generalizing solution. *Thus, hitting its sweet spot would be the target, or where that is unknown, at least avoiding these extremes.*

Furthermore, we can also consider a variant of MDS around initialization, by switching the trajectory map $\mathbf{C}$ to its relative version $\mathbf{C}_\tau$ at $\tau = 0$, resulting in $\omega_0 = \frac{1}{n^2}\, \mathbb{1}_n^\top \cdot \mathbf{C}_0 \cdot \mathbb{1}_n = \left\| \frac{1}{n}\, \widehat{\boldsymbol{\Theta}}_0^\top \mathbb{1}_n \right\|^2$, where $n = |\mathcal{T}_0|$. This can be useful when the initialization is rather distant from the origin, and

[1] In practice, such sub-sampling will indeed be required to avoid extremely high storage costs to checkpoint the parameters for each point, and the sub-sampling interval will be typically in epochs.

might wash off the directional nature of the trajectory.

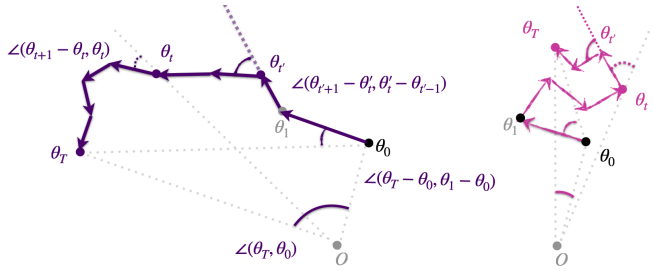

Figure 1. Illustration of two trajectories and angular measures.

(ii) *Angular Measures:* One such key measure would be the angle between consecutive (net) updates, i.e., $\angle(\boldsymbol{\theta}_{t+1}-\boldsymbol{\theta}_t, \boldsymbol{\theta}_t-\boldsymbol{\theta}_{t-1})$. Next, we can consider a cone with the vertex at initialization and track its apex angle in the form of $\angle(\boldsymbol{\theta}_t-\boldsymbol{\theta}_0, \boldsymbol{\theta}_1-\boldsymbol{\theta}_0)$. Likewise, we can also consider a cone at origin and compute the apex angle there, $\angle(\boldsymbol{\theta}_t, \boldsymbol{\theta}_0)$. This measure at origin will give us an idea of the amount of directional movement across a global scale, while the one centered at the initialization will indicate a more local or relative scale.

(iii) *Norm-based Measures:* Besides, we will also include other previously reported measures of lengths that are relevant in this respect, such as: parameter norms $\|\boldsymbol{\theta}_t\|_2$, distance from initialization $\|\boldsymbol{\theta}_t-\boldsymbol{\theta}_0\|_2$, norm between consecutive points $\|\boldsymbol{\theta}_{t+1}-\boldsymbol{\theta}_t\|_2$.

Remark. For extremely large neural networks, with several billions of parameters, building the underlying kernel matrices can start being a tad bit resource-expensive. In principle, there is a rich body of work in kernel methods that has focused on developing efficient approximations (Davis et al., 2014; Chen et al., 2021). But, as we foray into this novel trajectory perspective, we do not resort to such approximations and compute measures exactly for the sake of accuracy.

3. A Tale of Hyperparameters

There is an emerging folk intuition in the research community that, over the past decade, networks have co-evolved hand-in-hand, amidst other things, with a certain particular set of optimizers and hyperparameter choices, deviating from which tends to produce significantly poor results. Let us see one such case in action, for the case of ResNet50 trained on ImageNet with SGD, achieving the familiar top-1 accuracy of $\sim 76\%$. Further, as is usual convention, this network was trained via a learning rate $\eta = 0.1$, momentum $\mu = 0.9$, batch size $B = 256$, weight decay $\lambda = 0.0001$ for 90 epochs, with a multiplicative decay by a factor of 0.1 at epochs 30 and 60.

Visual Tour of the Trajectory. Before we start this excursion with the hyperparameters, let us simply pay a glance at the nature of the optimization trajectory, as visualized via the proposed qualitative hallmark, namely the trajectory map $\mathbf{C}$. In particular, we save checkpoints from the initialization until the final epoch, at intervals of every epoch, and thereby giving us a total of 91 checkpoints. We plot this 91×91 matrix in Figure 2.

For starters, we can easily make out three[2] distinct phases of optimization which is marked by an increased darkening of the pixels and their locations are precisely where learning rate decay was applied. The onset of these phases also seems to bring about an increased cosine similarity of the parameters contained within these phases, which seems to imply that following the learning rate decay the optimization is honing into a progressively confined subspace of the landscape.

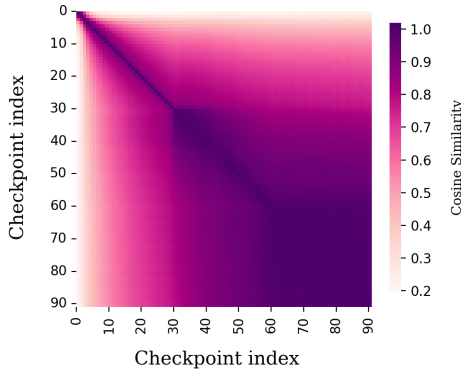

Figure 2. Trajectory Map of ResNet50 on ImageNet, $\omega = 0.764$.

Next, the mean directionality score (MDS) for this particular figure comes out to be $\omega = 0.764$. To contextualize this value, we should remind ourselves that we are working in a space of ~ 25.6 million dimensions. This should serve to emphasize that network optimization trajectories are highly structured, and not merely random points in high-dimensions whose cosine similarity goes to zero. As a further note, the cosine similarity of two different instantiations of the ResNet50 parameters, from the same (and the usual) random initialization scheme, gives a value[3] of 0.374. However, besides these comparisons, it is still somewhat unclear what the value of MDS tells us about the trajectory. In particular, we need to ask ourselves (i) How does it rank in comparison to possibly other trajectories? (ii) Is it a high

[2] If we look closely, there seems to be another phase transition neighbouring the initialization and the subsequent couple of epochs, giving rise to a thin horizontal and vertical sliver of relatively lighter colour in this figure.

[3] A reason for this high value of cosine similarity is the presence of BatchNorm or LayerNorm learnable scale parameters, which are typically initialized to all ones.

enough value, or should we aim for something much larger? (iii) But since the maximum value of ω can be 1 and since we have initialization in the mix here, obtaining such a value would not be so desirable as it would effectively mean the absence of any feature learning (Chizat et al., 2020), which seems to be a critical component behind the success of deep learning.

To better address these and other burning questions, let us now tinker slightly with certain hyperparameters. In particular, we will only touch just two of them, namely, momentum and weight decay, and turn them off one at a time. Importantly, everything else remains fixed. The ensuing trajectory maps can be found in Figure 3, where either momentum is turned off ($\mu = 0$) or weight decay ($\lambda = 0$) or both ($\mu = 0, \lambda = 0$). The first thing that stands out is that the trajectory maps become darker in colour, suggesting an increased cosine similarity, and especially the subfigure without both momentum and weight decay looks rather conspicuous, with essentially just one dark grid of extremely large cosine similarities. In particular, if we calculate the mean directional similarities, they turn out to be $\omega = 0.901, 0.931, 0.979$, respectively. It would also be worth noting that their top-1 accuracies are, $72.63\%, 70.86\%, 68.73\%$, with a net drop of about 10% by just turning off these two hyperparameters.

These results would indicate that the optimization hyperparameters seem to be leading to qualitatively different solutions, with the presence of weight decay or momentum encouraging more directional exploration, whereas in their absence, the optimization latches on to a nearby solution (at least, in a directional sense) and then short-circuits itself into a 'dead end'. However, these results also seem to run against the simplistic pictures one might conceive of regarding momentum and weight decay. For instance, intuitively, the use of momentum should add strength to the previous gradient directions and lead to increased directional similarity, but we find the opposite to hold. Similarly, in the absence of weight decay, the network is not constrained to remain in a ball around the origin and, in principle, there should be more license to explore in the landscape. Or, what are these intuitive notions not taking into account?

4. A Ride with Momentum, Decay, & More

In order to obtain a more refined understanding of the above observation, we would like to inspect in detail the angular and norm-based measures of the trajectory. Let's start by taking a look at how aligned are the net or the aggregate updates[4] in the presence of these hyperparameters and otherwise.

4.1. Momentum and the Angle between Updates

In particular, in Figure 4(a), we plot the angle between consecutive epochs, i.e, $\angle(\theta_{t+1} - \theta_t, \theta_t - \theta_{t-1})$. Interestingly, we find that this angle becomes obtuse a short while into the training process, and as a matter of fact, this angle is larger when momentum is turned on versus when off. Moreover, rather visibly, this increase in angle is larger when weight decay is also enabled, suggesting that weight decay and momentum are closely intertwined. Taken as such, this observation would point as to how the MDS increases when these hyperparameters are switched off. But, we would still like to gain a somewhat better understanding of this mechanism, even though doing so in precise details might be out of reach. Hence, we turn to the simplest and oft-employed model of a quadratic problem, and see where do we arrive.

Lemma 1. *Given a quadratic problem with ℓ_2 regularization of strength $\alpha > 0$, namely,*

$$\min_{\boldsymbol{\theta} \in \mathbb{R}^d} \frac{1}{2} \boldsymbol{\theta}^\top \mathbf{M} \boldsymbol{\theta} + \frac{1}{2} \alpha \|\boldsymbol{\theta}\|^2 ,$$

with $\mathbf{M} \in \mathbb{R}^{d \times d}$ symmetric with eigenvalues $\lambda_1 \geqslant \cdots \lambda_d$, the angle between successive steps $\Delta_t = \boldsymbol{\theta}_t - \boldsymbol{\theta}_{t-1}, \Delta_{t+1} = \boldsymbol{\theta}_{t+1} - \boldsymbol{\theta}_t$, when using gradient descent with a one-step momentum ($\mu > 0$) and learning rates η_t, η_{t+1}, can be upper and lower bounded as follows:

$$\langle \Delta_t, \Delta_{t+1} \rangle \leqslant \eta_t \eta_{t+1} (1 - \mu \eta_t - \eta_t \alpha - \eta_t \lambda_d)(\lambda_d + \alpha)^2 \|\boldsymbol{\theta}_{t-1}\|^2$$
$$\langle \Delta_t, \Delta_{t+1} \rangle \geqslant \eta_t \eta_{t+1} (1 - \mu \eta_t - \eta_t \alpha - \eta_t \lambda_1)(\lambda_1 + \alpha)^2 \|\boldsymbol{\theta}_{t-1}\|^2$$

Proof. See Appendix A. □

The above proof inherently considers the solution at $\boldsymbol{\theta}^\star = \mathbf{0}$, but if that is not the case, we can substitute for it in the objective and our derived upper and lower bounds would scale in the squared distance to the solution, i.e. $\|\boldsymbol{\theta}_{t-1} - \boldsymbol{\theta}^\star\|^2$. Besides, in the above proof, we consider a one-step momentum, which inherently means resetting the momentum after every 2 steps. This is done for convenience, as our main purpose is to anyways gain insights into the phenomenon and not provide its ultimate proof.

Turning to the bounds themselves, notice that if the learning rate $\eta_t \geqslant 1/(\lambda_1 + \mu + \alpha)$, the lower bound will turn negative and will be multiplied by a factor of $(\lambda_1 + \alpha)^2 \|\boldsymbol{\theta}_{t-1}\|^2$. On the other hand, while the first term of the upper bound might still be positive, importantly, it is scaled by a factor of $(\lambda_d + \alpha)^2 \approx \alpha^2$ for matrices $\mathbf{M}$ which are close to degenerate.

Low-rank Hessian and Edge of Stability. In our context, the Hessian of the loss with respect to the parameters will

[4] We qualify this by 'net' or 'aggregate' as we are working on somewhat coarser granularity (i.e., 1 epoch) than actual updates or steps. But our current granularity is still rich enough to allow for the presented trends to persist even if go $2\times$ to $5\times$ more coarser.

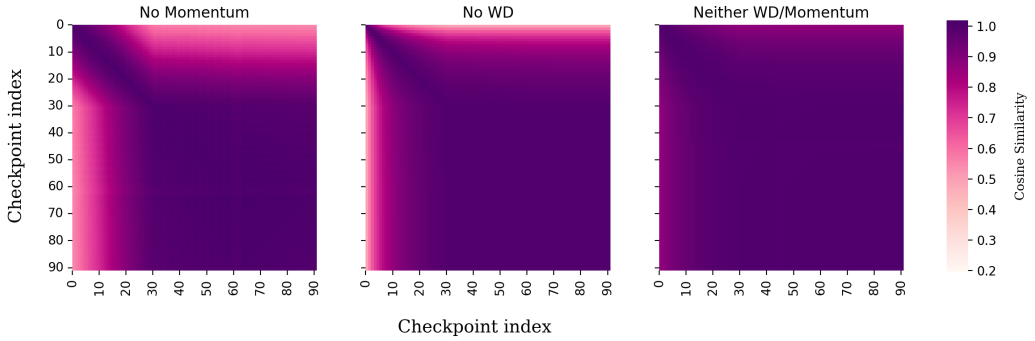

Figure 3. Trajectory Maps of ResNet50 trained on ImageNet without momentum or weight decay or both. The scale of cosine similarity is adjusted to match the values in Figure 2 and allows for a direct comparison. The values of MDS are, $\omega = 0.901, 0.931, 0.979$ respectively.

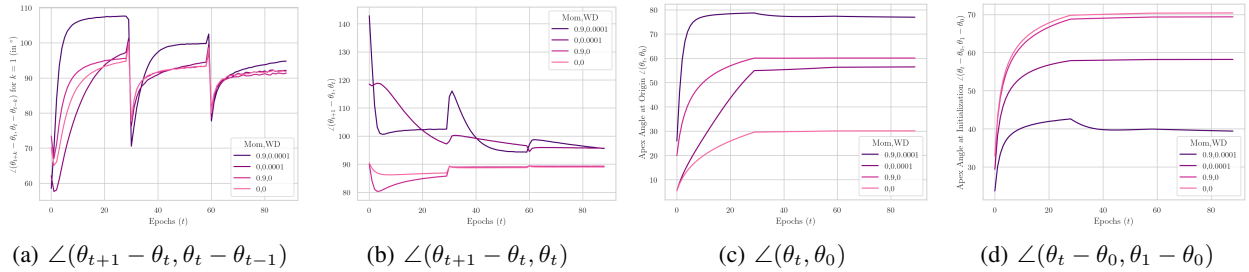

(a) $\angle(\theta_{t+1} - \theta_t, \theta_t - \theta_{t-1})$ (b) $\angle(\theta_{t+1} - \theta_t, \theta_t)$ (c) $\angle(\theta_t, \theta_0)$ (d) $\angle(\theta_t - \theta_0, \theta_1 - \theta_0)$

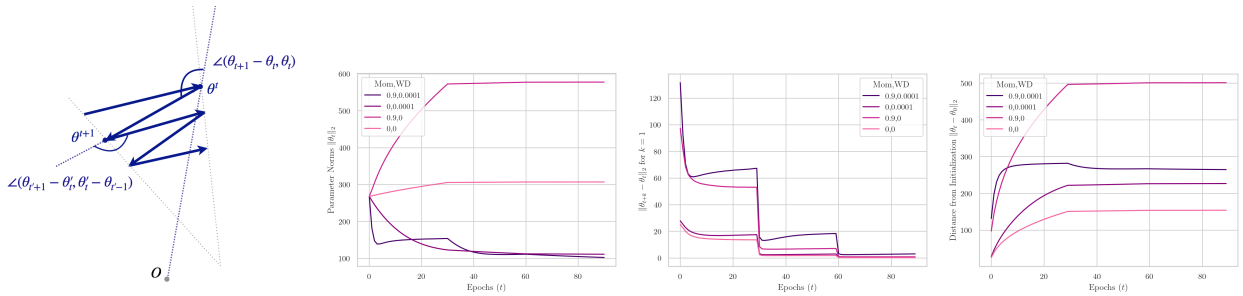

(e) Illustration of EoS with Momentum (f) $\|\theta_t\|_2$ (g) $\|\theta_{t+k} - \theta_t\|_2$ (h) $\|\theta_t - \theta_0\|_2$

Figure 4. Angular and Norm-based measures: ResNet50, ImageNet, Momentum and Weight Decay

play the role of the matrix $\mathbf{M}$, since we can assume a second-order Taylor series will hold across the two steps. But it is also known through prior empirical work that the Hessian is significantly degenerate (Sagun et al., 2017), which has also been proven rigorously for deep linear fully-connected and convolutional networks (Singh et al., 2021). Furthermore, this requirement on the learning rate η_t is actually looser than the adaptivity of the largest eigenvalue of the Hessian to the learning rate $\lambda \approx \frac{2}{\eta}$, as shown in the recent work on Edge of Stability (EoS) (Cohen et al., 2022).

Explaining the Obtuse angles. Owing to these facts, we will have that $\lambda_d(\mathbf{M}) \approx 0$, and which further implies that the upper bound on the inner-product between the updates will be approximately zero, and the lower-bound will be large in absolute value and negative. Therefore, this explains how the angles between consecutive epochs can turn out to be obtuse. More broadly, the obtuse angle indeed implies that there are oscillations, especially along the direction of the largest Hessian eigenvector. Further, from Lemma 1, we see that the magnitude of the inner-product of the updates scales in proportion to η_{t+1}. Hence, a way to dampen the oscillations[5] is to decrease the learning rate, and as can be seen in Figure 4(a), the learning rate decay at epochs 30 and 60 is followed right after with the angles turning from obtuse to acute. Lastly, here in the constraint on the

[5]These oscillations need not necessarily translate into gross instabilities at the level of the loss, since as can be seen in Figure 4(g), the update norms progressively shrink in each of the three learning rate phases.

learning rate (the additive terms α and μ), we can also see how momentum and weight decay go hand-in-hand, each accentuating the effect of the other.

Towards a holistic picture of Momentum. Besides, in Figure 4(c) and 4(d), we find that in the presence of momentum, a larger angle is traced at the origin by the trajectory, suggesting a more directional exploration, while the angle traced at initialization is smaller. The latter can also be seen from Figure 4(h), since with momentum, the trajectory moves further away from the initialization. Apart from this, in the absence of weight decay, the updates seem to be strengthening with momentum and the parameter norm rises 4(f) as well, giving rise to a mental picture of a trajectory similar to that left purple trajectory in Figure 1, at least until the training hits EoS.

With weight decay, as there is a decrease in parameter norm Figure 4(f) alongside the EoS process, as well as due to the presence of larger obtuse angles, we expect a reasonable affinity with our illustration in Figure 4(e), where we see the updates oscillating and slowly drifting towards the origin O below.

4.2. More than just Weight Decay

Now that we have gained a richer understanding of momentum and its interaction with weight decay, let us turn to weight decay alone and understand its sole effect on the directional nature of the trajectories. We already noticed the increase in mean directional similarity (MDS) when weight decay is disabled for ResNet50, trained with SGD on ImageNet. In fact, we find a similar effect if switch to an adaptive optimizer, like AdamW (Loshchilov & Hutter, 2017), the trajectory maps for which can be found in Figure 5. Here, we used regularization constants from $\lambda = 0$ until the first value where we witness a decrease in test performance, which in this case was $\lambda = 1$. Specifically, we analyze the weight decay coefficients in $\lambda \in \{1, 0.1, 0.01, 0.001, 0\}$. The corresponding MDS come out to be, $\omega = 0.731, 0.679, 0.844, 0.882, 0.885$.

We notice that, as before, increasing weight decay leads to a heightened directional exploration, or lower MDS. Except for the case of $\lambda = 1$, which seems to be a slight anomaly. If we take a look at its corresponding trajectory map in Figure 5, we find that there is a much darker square grid that onsets around epoch 30. But also here we find increased cosine similarities in a larger band around the diagonal, relative to the case of $\lambda = 0.1$. As it turns out, with such a high weight decay coefficient $\lambda = 1$, this particular network underfits, achieving a train/test top-1 accuracy as $54.63\%, 50.52\%$ respectively. This fact can also be confirmed by the plots of distance from initialization and the apex angle at initialization, which are located in Appendix C.3. The performance for the rest of the networks improves, more or less, as expected with weight decay, and in particular, achieve accuracies of $75.45\%, 73.38\%, 71.03\%, 71.41\%$. Furthermore, in such a case of underfitting, we notice that computing the relative MDS from initialization corrects for the underfitting itself, resulting in the values of ω_0 as $0.985, 0.807, 0.862, 0.897, 0.900$ for $\lambda = 1, 0.1, 0.01, 0.001, 0$ respectively.

Having reaffirmed our results extensively for this setting, let us understand how directional exploration is encouraged by weight decay. The Figure 7 gives a physics-based intuition into this aspect. In particular, we can think of the loss gradient pulling the network parameters rightwards, while the force exerted by weight decay tries to pull the network downwards. The relative strengths of these two 'forces' have been represented by the lengths of the two vector arrows. We notice that as the weight decay strength is increased, from the left subfigure to the right, the angle traced at the origin (O) also increases. This quite simply explains how weight decay can contribute towards directional exploration.

4.3. Directional Effects in Other Key Settings

In addition to the momentum and weight decay, there are other crucial hyperparameters, such as learning rate and batch size, whose directional effects warrant a mention. We carry out additional experiments in these settings, and from where, the key findings are that the **learning rate**, as it would be easy to guess, indeed encourages directional exploration leading to low MDS scores. But, somewhat more interestingly, we find that increasing the **batch size** also helps further exploration and thereby decreases the MDS scores. The trajectory maps can be found in the Figure 6 While we encourage the curious reader to have a look at the Appendix C.11, we find that with increased batch size, the angle between the updates as well as the angle between the update and the current location become increasingly obtuse, and thus making room for a wider directional exploration. In contrast, for smaller batch sizes these angles are closer to 90°. We hypothesize that a similar mutual interaction, as observed with weight decay and momentum, also occurs with batch size is considered. A detailed analysis, however, remains outside the current scope.

Lastly, we also experimented with **Sharpness-Aware Minimization** (Foret et al., 2021) (SAM), where we found that a higher value of the SAM regularization coefficient leads to a slightly increased directional similarity, which could potentially be related to SAM directing optimisation to flatter basins wherein the individual points are more directionally alike and have higher cosine similarities. The detailed results can be found in the Appendix C.5.

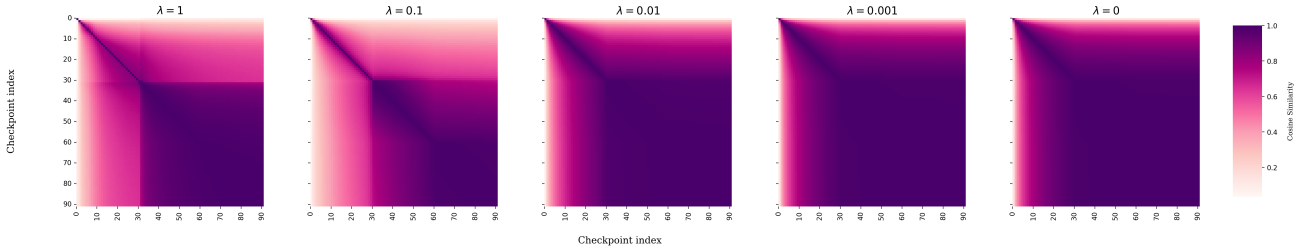

Figure 5. Trajectory Maps of ResNet50 for varying models across different amounts of Weight Decay, with the corresponding MDS scores being $\omega = 0.731, 0.679, 0.844, 0.882, 0.885$.

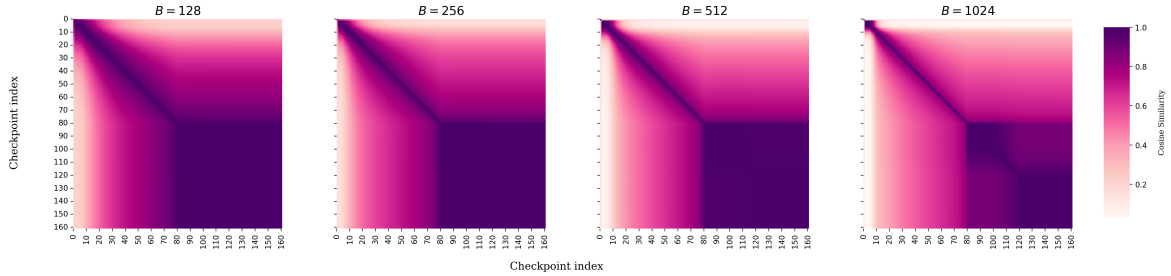

Figure 6. Trajectory Maps of VGG16 models across different batch sizes. The learning rates have been scaled in proportion to the batch size, and the training schedule was adjusted to ensure an equal number of steps (and not simply epochs) for all the runs. We also adjusted the learning rate schedule to drop learning rates at a corresponding number of steps across the experiments. The respective MDS values are $\omega = 0.753, 0.723, 0.660, 0.619$ and the test accuracies are $91.63\%, 91.82\%, 92.44\%, 92.39\%$.

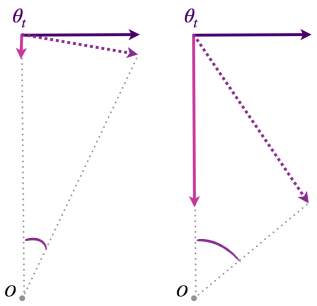

Figure 7. Directional Exploration due to Weight Decay. The pink downward vector represents the pull towards the origin (O) due to an energy corresponding to the norm squared of the parameters, while the leftward vector in purple represents the force due to the objective energy (classification loss).

Other Settings and Datasets. As a final remark for this section, we would like to emphasize that similar results for weight decay as well as momentum, can be found under different hyperparameter settings in the supplementary material. In particular, we analyze the qualitative and quantitative hallmarks for multiple values of learning rate, weight decay, and momentum for VGG16 on CIFAR10 as well as other values for momentum and weight decay in the case of ResNet50 trained with SGD, and even Vision Transformer trained with AdamW on ImageNet across varying weight decay, but these have to be omitted here due to space constraints.

5. Hauling Trajectory Hallmarks for LLMs

Having covered rather extensively, the crucial set of hyperparameters as well as optimizers, the one question that would still be on the minds of readers: how does it behave with scale? With all the massive improvements wrought in by Large Language Models (LLMs) and their impressive scaling behaviour, it would be relevant to uncover the structure of trajectories across models of different sizes. Several questions arise: (a) Do we see similar patterns in trajectories of networks trained on language modelling tasks? (b) What is their trend over increasing model sizes? (c) Do we expect increasing parameter scale to provide new directions for learning or do we expect scale to regularize the occurrence of complex trajectories?

Thanks to Pythia's (Biderman et al., 2023) publically released model checkpoints over training, for GPT-NeoX (Black et al., 2022) models — ranging in sizes from 14 Million (M) to 12 Billion (B) — we can provide answers into the above questions. Given that processing all of the available checkpoints would require several terabytes of cache, we select every fourth check-

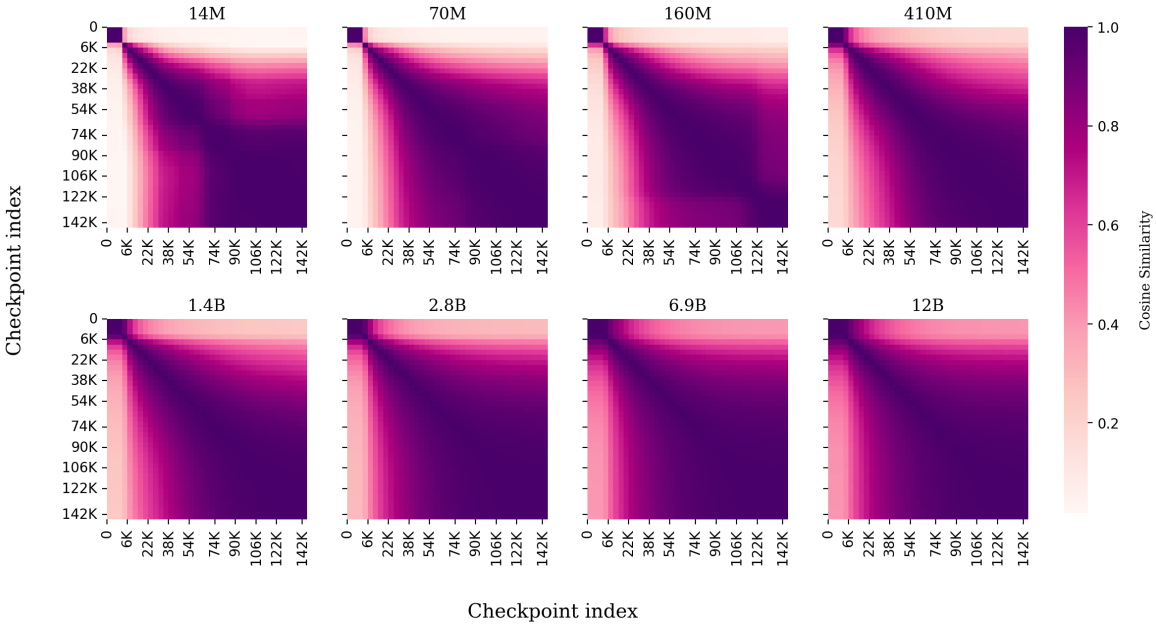

Figure 8. Trajectory Maps of Pythia GPT-NeoX models across two orders of model scales trained on Pile. The corresponding MDS values are $\omega = 0.650, 0.672, 0.678, 0.726, 0.759, 0.786, 0.818, 0.815$.

point, resulting in 39 checkpoints that we analyze for models of sizes: 14M, 70M, 160M, 410M, 1.4B, 2.8B, 6.9B, 12B. The results for these experiments can be found in Figure 8, with the corresponding MDS being: $\omega = 0.650, 0.672, 0.678, 0.726, 0.759, 0.786, 0.818, 0.815$.

First, we note that there is a tiny square grid in the upper-left corner, which delineates precisely the learning rate warmup phase. Next, the subsequent larger grid starts out, for 14M, with distinct subgrids but then over increasing model scale takes a funnel-like shape around 410M, before becoming rather homogeneous by 12B parameters. Even the horizontal and vertical slivers corresponding to warmup and the rest of the epochs start to assume a higher cosine similarity with scale. Overall, increasing scale lends an intense dark hue to the trajectory maps, which seems to offer a concrete hypothesis the inductive bias of scale might be related to regularizing the trajectories.

Why do parameters become aligned with scale? A Theoretical Argument. We show that this surprising finding about the progressive increase in cosine similarity with scale has a relatively simple explanation, at least in the case of the large-width limit of deep networks. The gist of our argument is that *in the large width limit, any parameter updates that lead to stable feature updates must necessarily yield updated parameters that are identically aligned with their initialisation.* This is a well-known fact for lazy learning regimes like the Neural Tangent Kernel (Jacot et al., 2020) or standard parameterisations, where no feature learning occurs. What may be surprising is that this is necessarily true for feature learning regimes like μP (Yang et al., 2022). The precise details can be found in Appendix B.

6. Related Work and Discussion

Directional Convergence. Prior work has theoretically noted a notion of directional convergence (Ji & Telgarsky, 2020), wherein the parameters of simple networks and classifiers converge quickly, in terms of their direction. Likewise (Merrill et al., 2020) have observed that cosine similarity between subsequent parameter checkpoints during T5 (Raffel et al., 2023) pre-training rapidly approaches 1. Our analysis of the trajectory maps can thus be seen as related to this aspect, however, we carry out a comprehensive analysis of how directional similarity of the parameters evolves over the course of training, how it behaves in a variety of relevant settings triggered by enabling or disabling key hyperparameters, and how it varies across models of unprecedented scales. Moreover, our analysis of the trajectory via the quantitative and qualitative hallmarks provides a more refined and insightful picture of the nature of optimization trajectory, instead of the mere fact about the rapid directional convergence noted in prior works.

Implicit Effects of Hyperparameters. Implicit bias (Gunasekar et al., 2018; Li et al., 2019; 2020; Moroshko et al., 2020) has emerged as one of the main contenders for explaining the success of deep neural networks. This principle, or ideology, has also inspired several works which

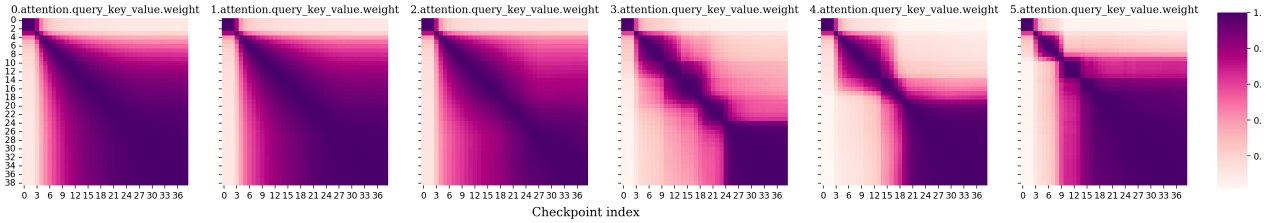

Figure 9. Layerwise Trajectory Maps for Q,K,V weights across depth fot GPT-NeoX trained on Pile for the 14M model.

seek to uncover the implicit effects that might be latent in the regular working of hyperparameters. To name a few, Andriushchenko et al. (2023) for instance suggest a loss stabilization mechanism behind weight decay, while Liu et al. (2023) attempt to characterize the implicit bias of large learning rates in terms of resulting in a flatter solution, and Jelassi & Li (2022); Cao et al. (2023) explain the implicit bias of momentum and batch normalization with regards to margin. In contrast, we take a broad and general perspective by adopting a full trajectory view. In particular, we explore more deeply an intriguing interaction of various optimization knobs, such as that between momentum and weight decay, and show its link with Edge of Stability (Cohen et al., 2022).

Complexity of Optimization Path as a Generalization Measure? There has been, of course, a huge set of works analyzing the generalization behaviour but with more of a focus on final basin quality measures, like sharpness (Zhang et al., 2021; Petzka et al., 2021; Singh et al., 2022; Gastpar et al., 2023). While apriori, we might believe that the final basin quality matters more than the particular path taken to reach it (however complex the path might be). But, thinking about the implicit bias (whatever that truly is), which is at play when optimizing over-parameterized networks, and considering our empirical findings about the trajectory maps when the hyperparameters are tweaked, it seems that the kind of optimization path followed might matter more than the eventual destination. In fact, our notion of the mean directional score (MDS) has shown promise to be a useful measure to track the quality of optimization, given its well-behaved nature in various controlled settings. While, here our primary focus was to reveal, much more broadly, the varied characteristics of the optimization trajectory, it would form, without a doubt, a fascinating question to explore MDS as an alternative correlator/predictor of generalization in future work.

Mechanistic Understanding of Neural Networks and LLMs. Besides, our analysis can also pave the way for a novel data-free mechanistic understanding of LLMs (see for instance, Figure 9, where the query-key-value weights for the middle layer interestingly converge the latest; Appendix E contains the entire set of figures.). This holistic optimization path perspective can complement the top-down approach of mechanistic understanding of LLMs via influence functions (Grosse et al., 2023) and the bottom-up circuit view of Transformers (Elhage et al., 2021).

Exploiting Redundancy in Optimization. Lastly, given the high cosine similarity between the parameter checkpoints, this raises the exciting prospect of exploiting the structure of optimization trajectories for faster optimization, like via a line search (Vaswani et al., 2019) or adapting only scalar parameters per layer (Frankle et al., 2021) such as those in LayerNorm. Further, by carrying out a layerwise directional analysis, we might be able to 'pause' optimization at the level of certain layers or blocks of parameters a little while into training, or simply, intersperse their updates at some intervals. All in all, this would allow for a more structured form of efficient low-rank training (Hu et al., 2021) in otherwise extremely high dimensional spaces.

7. Conclusion

In sum, we present and develop the perspective of studying the entire optimization trajectories, and their directional geometry, for analyzing the nature of solutions reached by neural networks (including LLMs) in different settings. More specifically, we consider qualitative and quantitative hallmarks (such as the trajectory map and angle between successive trajectory points, respectively), and utilize them to showcase the manner in which key hyperparameters and regularization techniques as well as the network scale affect the ensued optimization trajectories. Notably, we observe that increasing momentum, weight decay, batch size, and learning rate increase the extent of directional exploration in the trajectory, while sharpness-aware minimization and increased network scale have an implicit regularization effect of reducing the extent of directional exploration.

Nevertheless, we have merely scratched the surface of this trajectory perspective into understanding optimization and generalization behaviour in neural networks. We genuinely believe that there is a lot to be understood about the complex, intermingled behaviour of optimization in deep learning, and hopefully, this work will bring further nuance in these

areas and foster an understanding of the structure of these trajectories.

Impact Statement. If the directional redundancy present in the optimization paths of neural networks and large language models can be tapped, this would enable faster algorithmic techniques of training large networks quite efficiently and thereby help towards reducing the otherwise heavy carbon footprint of these models. Besides, the hallmarks of optimization trajectories that we presented can help towards furthering our understanding of the generalization aspects of these networks.

References

Andriushchenko, M., D'Angelo, F., Varre, A., and Flammarion, N. Why do we need weight decay in modern deep learning?, 2023.

Biderman, S., Schoelkopf, H., Anthony, Q. G., Bradley, H., O'Brien, K., Hallahan, E., Khan, M. A., Purohit, S., Prashanth, U. S., Raff, E., et al. Pythia: A suite for analyzing large language models across training and scaling. In *International Conference on Machine Learning*, pp. 2397–2430. PMLR, 2023.

Black, S., Biderman, S., Hallahan, E., Anthony, Q., Gao, L., Golding, L., He, H., Leahy, C., McDonell, K., Phang, J., et al. Gpt-neox-20b: An open-source autoregressive language model. *arXiv preprint arXiv:2204.06745*, 2022.

Cao, Y., Zou, D., Li, Y., and Gu, Q. The implicit bias of batch normalization in linear models and two-layer linear convolutional neural networks. In *The Thirty Sixth Annual Conference on Learning Theory*, pp. 5699–5753. PMLR, 2023.

Chen, Q., Zhao, B., Wang, H., Li, M., Liu, C., Li, Z., Yang, M., and Wang, J. Spann: Highly-efficient billion-scale approximate nearest neighbor search, 2021.

Chizat, L., Oyallon, E., and Bach, F. On lazy training in differentiable programming, 2020.

Cohen, J. M., Kaur, S., Li, Y., Kolter, J. Z., and Talwalkar, A. Gradient descent on neural networks typically occurs at the edge of stability, 2022.

Davis, D., Balzer, J., and Soatto, S. Asymmetric sparse kernel approximations for large-scale visual search. In *Proceedings of the IEEE Conference on Computer Vision and Pattern Recognition*, pp. 2107–2114, 2014.

Elhage, N., Nanda, N., Olsson, C., Henighan, T., Joseph, N., Mann, B., Askell, A., Bai, Y., Chen, A., Conerly, T., et al. A mathematical framework for transformer circuits. *Transformer Circuits Thread*, 1:1, 2021.

Foret, P., Kleiner, A., Mobahi, H., and Neyshabur, B. Sharpness-aware minimization for efficiently improving generalization, 2021.

Frankle, J., Schwab, D. J., and Morcos, A. S. Training batchnorm and only batchnorm: On the expressive power of random features in cnns, 2021.

Gastpar, M., Nachum, I., Shafer, J., and Weinberger, T. Fantastic generalization measures are nowhere to be found. *arXiv preprint arXiv:2309.13658*, 2023.

Grosse, R., Bae, J., Anil, C., Elhage, N., Tamkin, A., Tajdini, A., Steiner, B., Li, D., Durmus, E., Perez, E., Hubinger, E., Lukovsiūtė, K., Nguyen, K., Joseph, N., McCandlish, S., Kaplan, J., and Bowman, S. R. Studying large language model generalization with influence functions, 2023.

Gunasekar, S., Lee, J., Soudry, D., and Srebro, N. Characterizing implicit bias in terms of optimization geometry. In *International Conference on Machine Learning*, pp. 1832–1841. PMLR, 2018.

He, K., Zhang, X., Ren, S., and Sun, J. Delving deep into rectifiers: Surpassing human-level performance on imagenet classification. In *Proceedings of the IEEE international conference on computer vision*, pp. 1026–1034, 2015.

Hu, E. J., Shen, Y., Wallis, P., Allen-Zhu, Z., Li, Y., Wang, S., Wang, L., and Chen, W. Lora: Low-rank adaptation of large language models, 2021.

Jacot, A., Gabriel, F., and Hongler, C. Neural tangent kernel: Convergence and generalization in neural networks. *Advances in neural information processing systems*, 31, 2018.

Jacot, A., Gabriel, F., and Hongler, C. Neural tangent kernel: Convergence and generalization in neural networks, 2020.

Jelassi, S. and Li, Y. Towards understanding how momentum improves generalization in deep learning, 2022. URL https://openreview.net/forum?id=lf0W6tcWmh-.

Ji, Z. and Telgarsky, M. Directional convergence and alignment in deep learning. *Advances in Neural Information Processing Systems*, 33:17176–17186, 2020.

Langley, P. Crafting papers on machine learning. In Langley, P. (ed.), *Proceedings of the 17th International Conference on Machine Learning (ICML 2000)*, pp. 1207–1216, Stanford, CA, 2000. Morgan Kaufmann.

Li, Y., Ma, T., and Zhang, H. Algorithmic regularization in over-parameterized matrix sensing and neural networks with quadratic activations, 2019.

Li, Y., Wei, C., and Ma, T. Towards explaining the regularization effect of initial large learning rate in training neural networks, 2020.

Liu, C., Huang, W., and Xu, R. Y. D. Implicit bias of deep learning in the large learning rate phase: A data separability perspective. *Applied Sciences*, 13(6):3961, 2023.

Loshchilov, I. and Hutter, F. Decoupled weight decay regularization. *arXiv preprint arXiv:1711.05101*, 2017.

Merrill, W., Ramanujan, V., Goldberg, Y., Schwartz, R., and Smith, N. Effects of parameter norm growth during transformer training: Inductive bias from gradient descent. *arXiv preprint arXiv:2010.09697*, 2020.

Moroshko, E., Gunasekar, S., Woodworth, B., Lee, J. D., Srebro, N., and Soudry, D. Implicit bias in deep linear classification: Initialization scale vs training accuracy, 2020.

Petzka, H., Kamp, M., Adilova, L., Sminchisescu, C., and Boley, M. Relative flatness and generalization. In Beygelzimer, A., Dauphin, Y., Liang, P., and Vaughan, J. W. (eds.), *Advances in Neural Information Processing Systems*, 2021. URL https://openreview.net/forum?id=sygvo7ctb_.

Raffel, C., Shazeer, N., Roberts, A., Lee, K., Narang, S., Matena, M., Zhou, Y., Li, W., and Liu, P. J. Exploring the limits of transfer learning with a unified text-to-text transformer, 2023.

Sagun, L., Evci, U., Guney, V. U., Dauphin, Y., and Bottou, L. Empirical analysis of the hessian of over-parametrized neural networks. *arXiv preprint arXiv:1706.04454*, 2017.

Singh, S. P., Bachmann, G., and Hofmann, T. Analytic insights into structure and rank of neural network hessian maps. *Advances in Neural Information Processing Systems*, 34:23914–23927, 2021.

Singh, S. P., Lucchi, A., Hofmann, T., and Schölkopf, B. Phenomenology of double descent in finite-width neural networks. In *International Conference on Learning Representations*, 2022. URL https://openreview.net/forum?id=lTqGXfn9Tv.

Vaswani, S., Mishkin, A., Laradji, I., Schmidt, M., Gidel, G., and Lacoste-Julien, S. Painless stochastic gradient: Interpolation, line-search, and convergence rates. *Advances in neural information processing systems*, 32, 2019.

Yang, G., Hu, E. J., Babuschkin, I., Sidor, S., Liu, X., Farhi, D., Ryder, N., Pachocki, J., Chen, W., and Gao, J. Tensor programs v: Tuning large neural networks via zero-shot hyperparameter transfer, 2022.

Zhang, S., Reid, I., Pérez, G. V., and Louis, A. Why flatness does and does not correlate with generalization for deep neural networks, 2021.

A. Omitted Proofs

Lemma 2. *Given a quadratic problem with ℓ_2 regularization of strength $\alpha > 0$, namely,*

$$\min_{\boldsymbol{\theta}\in\mathbb{R}^d} \frac{1}{2}\boldsymbol{\theta}^\top \mathbf{M}\boldsymbol{\theta} + \frac{1}{2}\alpha\|\boldsymbol{\theta}\|^2 ,$$

with $\mathbf{M}$ symmetric, the angle between successive steps $\Delta_t = \boldsymbol{\theta}_t - \boldsymbol{\theta}_{t-1}, \Delta_{t+1} = \boldsymbol{\theta}_{t+1} - \boldsymbol{\theta}_t$, when using gradient descent with a one-step momentum ($\mu > 0$) and learning rates η_t, η_{t+1}, can be upper and lower bounded as follows:

$$\langle \Delta_t, \Delta_{t+1}\rangle \leqslant \eta_t\eta_{t+1}(1 - \mu\eta_t - \eta_t\alpha - \eta_t\lambda_d)(\lambda_d + \alpha)^2\|\boldsymbol{\theta}_{t-1}\|^2$$
$$\langle \Delta_t, \Delta_{t+1}\rangle \geqslant \eta_t\eta_{t+1}(1 - \mu\eta_t - \eta_t\alpha - \eta_t\lambda_1)(\lambda_1 + \alpha)^2\|\boldsymbol{\theta}_{t-1}\|^2$$

Proof. Given function $f(\boldsymbol{\theta}) = \frac{1}{2}\boldsymbol{\theta}^\top\mathbf{M}\boldsymbol{\theta} + \frac{1}{2}\alpha\|\boldsymbol{\theta}\|^2$, the gradient at $\boldsymbol{\theta}$ will be $\nabla f(\boldsymbol{\theta}) = (\mathbf{M} + \alpha\mathbf{I})\boldsymbol{\theta}$. Then at the first optimization step, we do

$$\boldsymbol{\theta}_t = \boldsymbol{\theta}_{t-1} - \eta_t(\mathbf{M} + \alpha\mathbf{I})\boldsymbol{\theta}_{t-1}$$

The particular update being $\Delta_t := \boldsymbol{\theta}_t - \boldsymbol{\theta}_{t-1} = -\eta_t(\mathbf{M} + \alpha\mathbf{I})\boldsymbol{\theta}_{t-1}$. The next update is similar, but now we also have to factor in the momentum,

$$\boldsymbol{\theta}_{t+1} = \boldsymbol{\theta}_t - \eta_{t+1}\left(\nabla f(\boldsymbol{\theta}_t) - \mu\eta_t(\mathbf{M} + \alpha\mathbf{I})\boldsymbol{\theta}_{t-1}\right)$$

$$\begin{aligned}\Delta_{t+1} := \boldsymbol{\theta}_{t+1} - \boldsymbol{\theta}_t &= -\eta_{t+1}\left((\mathbf{M} + \alpha\mathbf{I})\boldsymbol{\theta}_t - \mu\eta_t(\mathbf{M} + \alpha\mathbf{I})\boldsymbol{\theta}_{t-1}\right)\\ &= -\eta_{t+1}\left((\mathbf{M} + \alpha\mathbf{I})\boldsymbol{\theta}_{t-1} - \eta_t(\mathbf{M} + \alpha\mathbf{I})^2\theta_{t-1} - \mu\eta_t(\mathbf{M} + \alpha\mathbf{I})\boldsymbol{\theta}_{t-1}\right)\\ &= -\eta_{t+1}\left((1 - \mu\eta_t - \alpha\eta_t)\mathbf{I} - \eta_t\mathbf{M}\right)(\mathbf{M} + \alpha\mathbf{I})\boldsymbol{\theta}_{t-1}\end{aligned}$$

Now, let us evaluate the inner-product $\langle \Delta_t, \Delta_{t+1}\rangle$,

$$\langle \Delta_t, \Delta_{t+1}\rangle = \eta_t\eta_{t+1}\boldsymbol{\theta}_{t-1}^\top \underbrace{(\mathbf{M} + \alpha\mathbf{I})\left((1 - \mu\eta_t - \eta_t\alpha)\mathbf{I} - \eta_t\mathbf{M}\right)(\mathbf{M} + \alpha\mathbf{I})}_{\mathbf{Z}}\boldsymbol{\theta}_{t-1}$$

Now without loss of generality we can consider $\mathbf{Z}$ to be a diagonal matrix, as $\mathbf{Z}$ is symmetric since $\mathbf{M}$ is symmetric, we can consider its spectral decomposition $\mathbf{Z} = \mathbf{U}\mathbf{D}\mathbf{U}^\top$ and project $\boldsymbol{\theta}_0$ onto its eigenvectors contained in $\mathbf{U}$. With this the matrices in the middle are diagonal and we can commute them, which yields us the following matrix:

$$\mathbf{Z} = \operatorname{diag}\begin{pmatrix}(1 - \mu\eta_t - \eta_t\alpha - \eta_t\lambda_1)(\lambda_1 + \alpha)^2\\ \vdots\\ (1 - \mu\eta_t - \eta_t\alpha - \eta_t\lambda_d)(\lambda_d + \alpha)^2\end{pmatrix}$$

where, we have denoted the eigenvalues of $\mathbf{M}$ as $\lambda_1 \geqslant \cdots \geqslant \lambda_d$.

Since the inner product of the updates is a quadratic form, we can upper and lower bound it based on the maximum and minimum eigenvalues of $\mathbf{Z}$, thus giving:

$$\eta_t\eta_{t+1}\lambda_{\min}(\mathbf{Z})\|\boldsymbol{\theta}_{t-1}\|^2 \leqslant \langle \Delta_t, \Delta_{t+1}\rangle \leqslant \eta_t\eta_{t+1}\lambda_{\max}(\mathbf{Z})\|\boldsymbol{\theta}_{t-1}\|^2$$

Because of the above form of eigenvalues of $\mathbf{Z}$ (diagonal matrices have their eigenvalues as their diagonal entries), we will have:

$\lambda_{\max}(\mathbf{Z}) = (1 - \mu\eta_t - \eta_t\alpha - \eta_t\lambda_d)(\lambda_d + \alpha)^2$ and $\lambda_{\min}(\mathbf{Z}) = (1 - \mu\eta_t - \eta_t\alpha - \eta_t\lambda_1)(\lambda_1 + \alpha)^2$ □

B. Why cosine similarities increase with scale?

Note, we assume that the majority of the parameter norm lies in the square hidden matrices, and not the input or output layers. Moreover, we use o, O, Θ to denote standard mathematical notation with regards to scaling in the limit width $n \to \infty$. For vectors, this notation is entry-wise.

Suppose we have a hidden layer with input $x_0 \in \mathbb{R}^n$ for width n, that is acted on by (without loss of generality) a square matrix $W_0 \in \mathbb{R}^{n \times n}$ to give:

$$h_0 = W_0 x_0$$

We suppose x has $\Theta(1)$ entries, as is the case with standard initialisations/parameterisations (He et al., 2015). We suppose W_0 has i.i.d. elements with initialisation that is $O(1/\sqrt{n})$ in order to ensure that each element of the features h has entries $\Theta(1)$.

Now, if we take a gradient update with learning rate η on some downstream loss L that depends on h (and not W or x), we get:

$$W_1 = W_0 - \eta \mathrm{d}h \cdot x_0^\top$$

where $\mathrm{d}h = \frac{\partial L}{\partial h} \in \mathbb{R}^{n \times 1}$ is our feature derivative.

Then if we have new input x_1 (wlog $x_1 = x_0$), we have new features:

$$h_1 = x_1 W_1 = h_0 - n\eta \mathrm{d}h \cdot \frac{x_0^\top x_0}{n}$$

For our features to be stable (i.e. $\Theta(1)$) after the update, we need $n\eta \mathrm{d}h$ to be $O(1)$, because $\frac{x_0^\top x_0}{n} = \Theta(1)$ by assumption on x. NB: if $n\eta \mathrm{d}h = o(1)$ we have no feature learning (ie NTK regime (Jacot et al., 2018)), and if $n\eta \mathrm{d}h = \Theta(1)$ we have feature learning (ie μP (Yang et al., 2022)).

In any case, $\eta \mathrm{d}h = O(1/n)$ entry-wise, which means that $W_1 - W_0 = -\eta \mathrm{d}h \cdot x_0^\top$ has $O(1/n)$ entries, again by assumption on the scale of elements of x_0.

But because $W_0 = \Theta(1/\sqrt{n})$, the initialisation will elementwise-dominate the $O(1/n)$ update for the first training step (and more training steps follows by induction). As a result, the update $W_T - W_0$ will always be an order of at least $\sqrt{n}$ smaller than the initialisation, and hence the new parameters W_T will be exactly aligned with the initialisation W_0 for all T in the large width limit, i.e. the cosine similarities will be 1.

C. Experimental Results

C.1. ResNet50: Switching off the hyperparameters

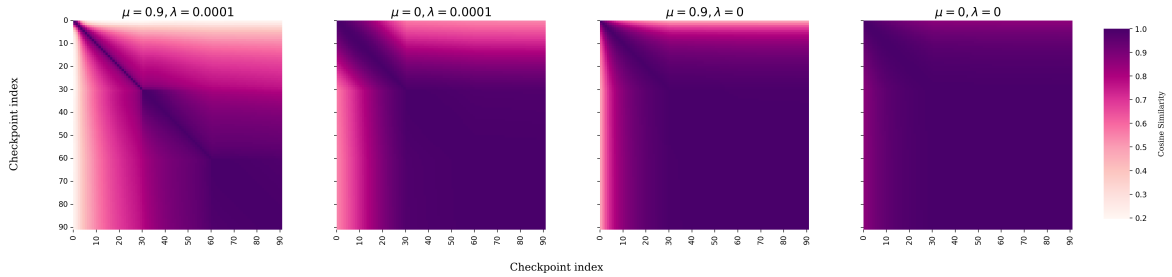

Figure 10. Trajectory Maps of ResNet50 models across different amounts of momentum and weight decay

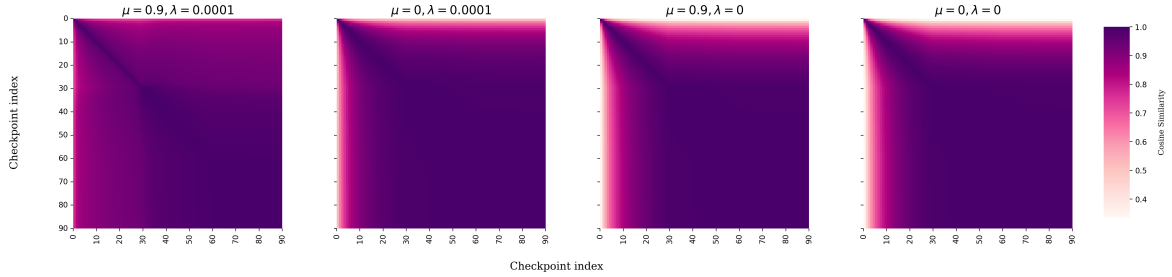

Figure 11. Relative Trajectory Maps, with respect to initialization, of ResNet50 models across different amounts of momentum and weight decay

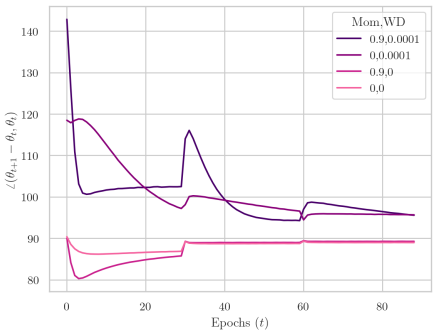

(a) $\angle(\theta_{t+1} - \theta_t, \theta_t)$

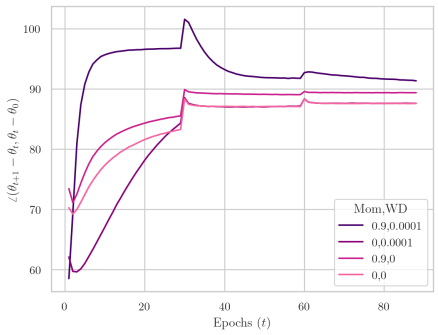

(b) $\angle(\theta_{t+1} - \theta_t, \theta_T - \theta_0)$

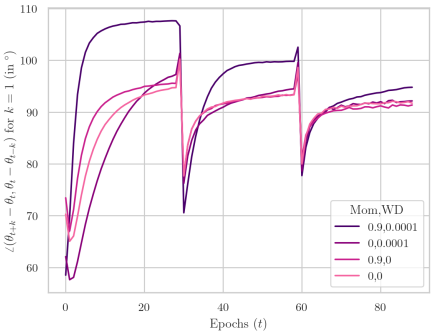

(c) $\angle(\theta_{t+k} - \theta_t, \theta_t - \theta_{t-k})$, for $k = 1$

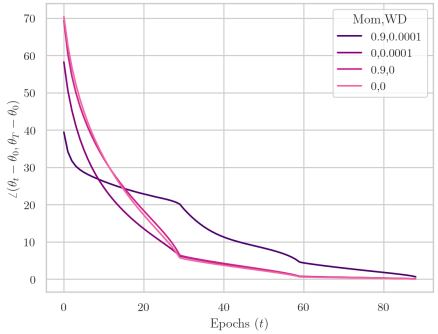

(d) $\angle(\theta_t - \theta_0, \theta_T - \theta_0)$

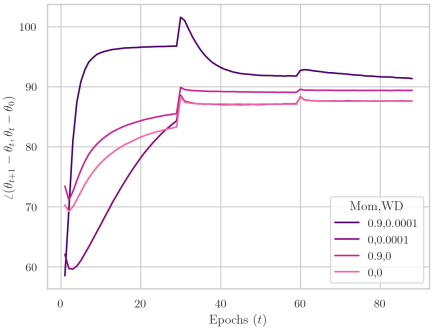

(e) $\angle(\theta_{t+1} - \theta_t, \theta_T - \theta_0)$

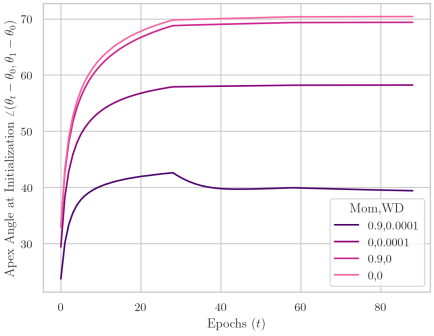

(f) Apex Angle at Initialization $\angle(\theta_t - \theta_0, \theta_1 - \theta_0)$

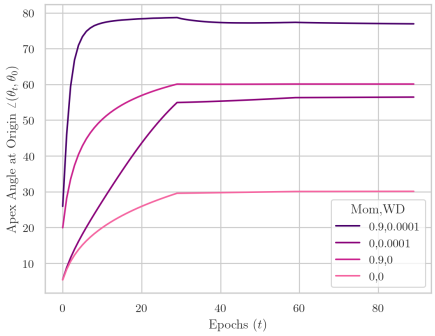

(g) Apex Angle at Origin $\angle(\theta_t, \theta_0)$

Figure 12. Angular measures of the Trajectory for ResNet50 trained on ImageNet

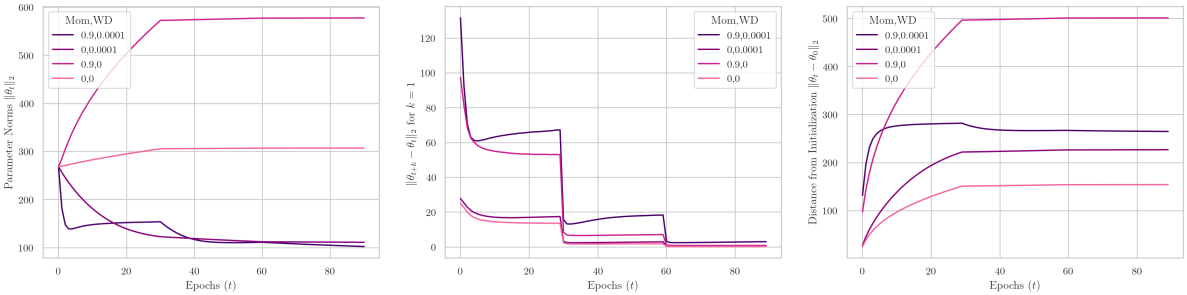

(a) $\|\theta_t\|_2$ (b) $\|\theta_{t+k} - \theta_t\|_2$ (c) $\|\theta_t - \theta_0\|_2$

Figure 13. Norm-based measures of the Trajectory for ResNet50 trained on ImageNet

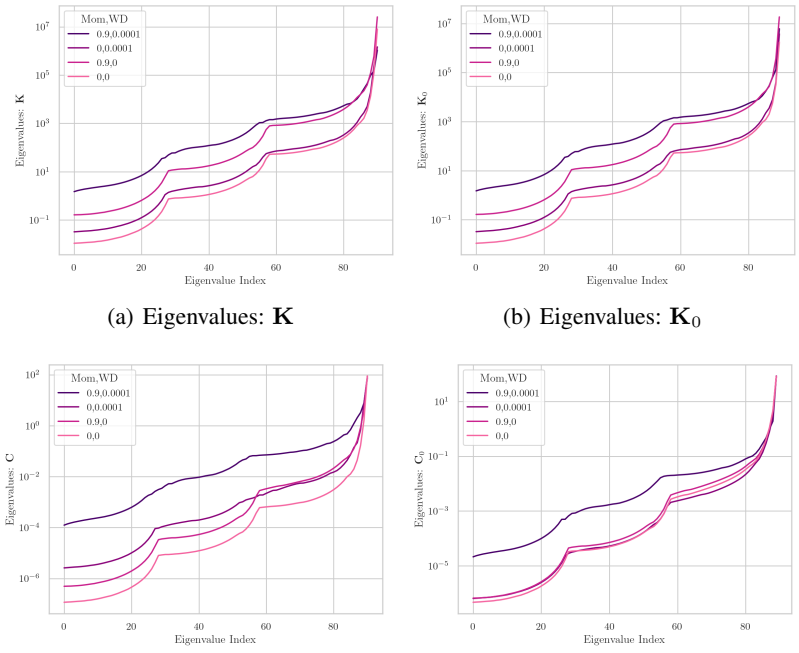

(a) Eigenvalues: $\mathbf{K}$ (b) Eigenvalues: $\mathbf{K}_0$

(c) Eigenvalues: $\mathbf{C}$ (d) Eigenvalues: $\mathbf{C}_0$

Figure 14. Spectral measures of the Trajectory for ResNet50 trained on ImageNet

C.2. ResNet50: Weight Decay, SGD

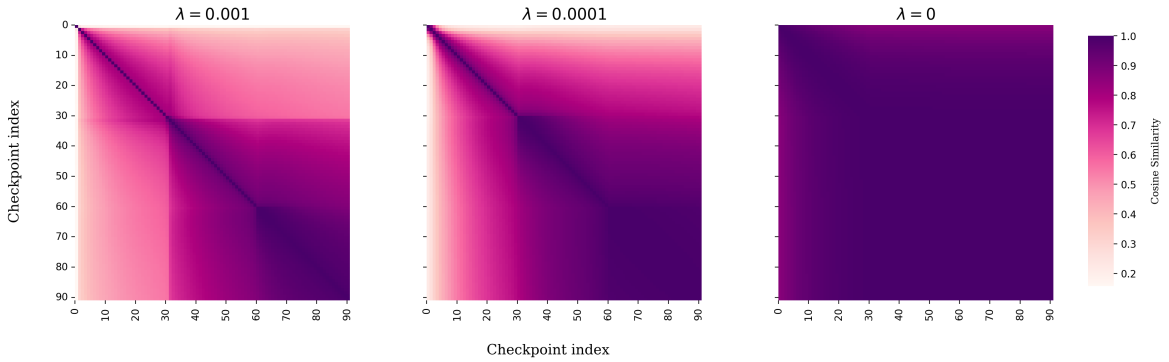

Figure 15. Trajectory Maps of ResNet50 models across different amounts of weight decay

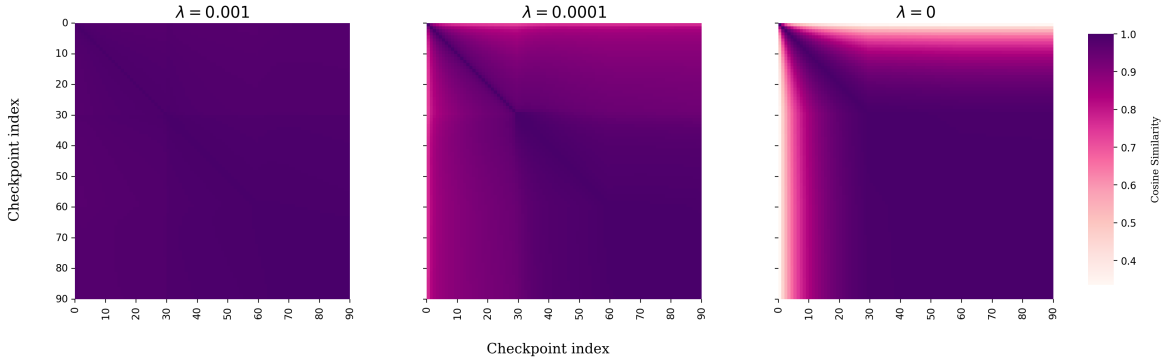

Figure 16. Relative Trajectory Maps, with respect to initialization, of ResNet50 models across different amounts of weight decay

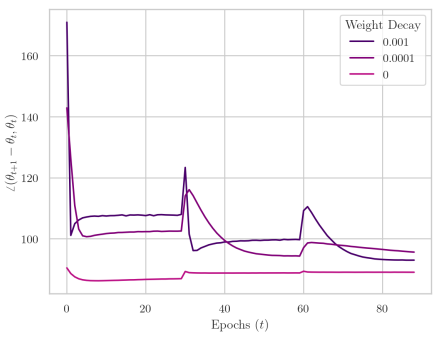

(a) $\angle(\theta_{t+1} - \theta_t, \theta_t)$

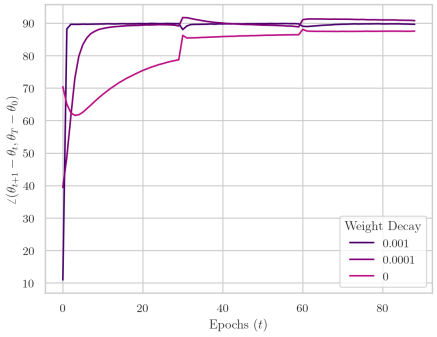

(b) $\angle(\theta_{t+1} - \theta_t, \theta_T - \theta_0)$

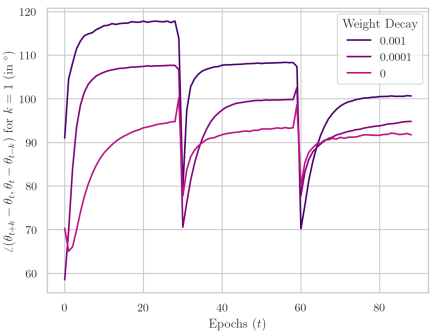

(c) $\angle(\theta_{t+k} - \theta_t, \theta_t - \theta_{t-k})$, for $k = 1$

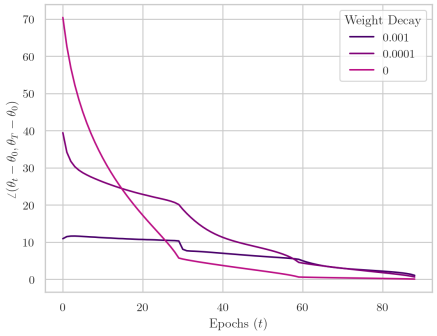

(d) $\angle(\theta_t - \theta_0, \theta_T - \theta_0)$

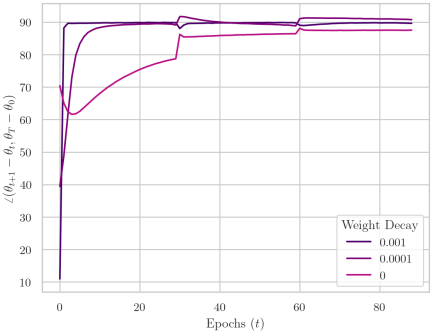

(e) $\angle(\theta_{t+1} - \theta_t, \theta_T - \theta_0)$

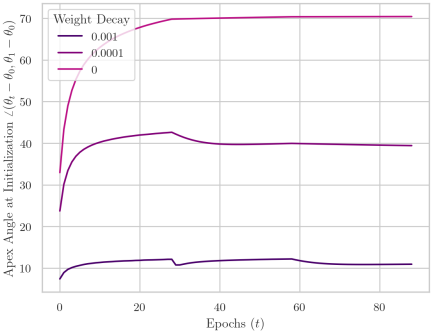

(f) Apex Angle at Initialization $\angle(\theta_t - \theta_0, \theta_1 - \theta_0)$

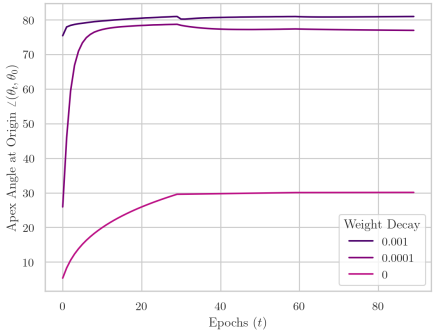

(g) Apex Angle at Origin $\angle(\theta_t, \theta_0)$

Figure 17. Angular measures of the Trajectory for ResNet50 trained on ImageNet

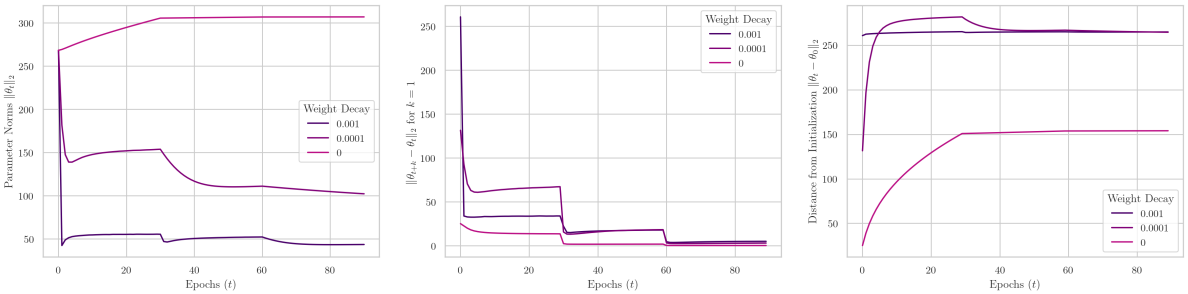

(a) $\|\theta_t\|_2$ (b) $\|\theta_{t+k} - \theta_t\|_2$ (c) $\|\theta_t - \theta_0\|_2$

Figure 18. Norm-based measures of the Trajectory for ResNet50 trained on ImageNet

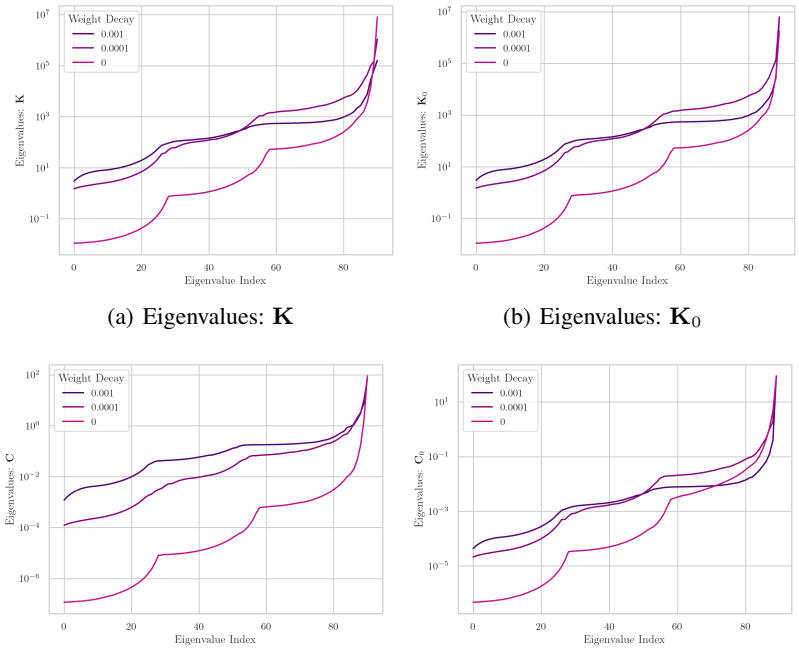

(a) Eigenvalues: $\mathbf{K}$ (b) Eigenvalues: $\mathbf{K}_0$

(c) Eigenvalues: $\mathbf{C}$ (d) Eigenvalues: $\mathbf{C}_0$

Figure 19. Spectral measures of the Trajectory for ResNet50 trained on ImageNet

C.3. ResNet50: Weight Decay, AdamW

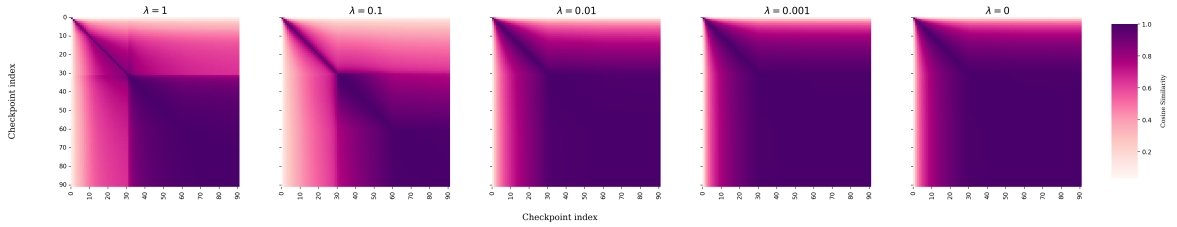

Figure 20. Trajectory Maps of ResNet50 models across different amounts of weight decay

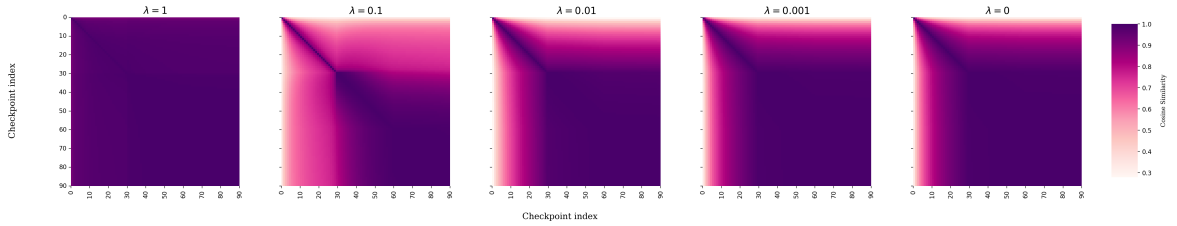

Figure 21. Relative Trajectory Maps, with respect to initialization, of ResNet50 models across different amounts of weight decay

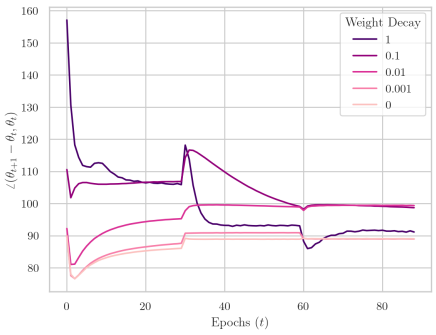

(a) $\angle(\theta_{t+1} - \theta_t, \theta_t)$

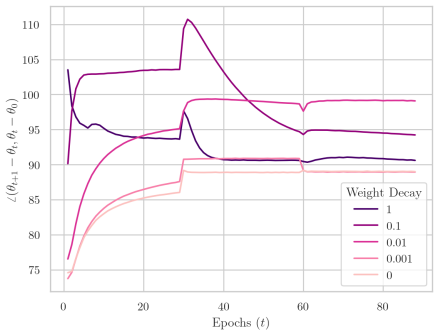

(b) $\angle(\theta_{t+1} - \theta_t, \theta_T - \theta_0)$

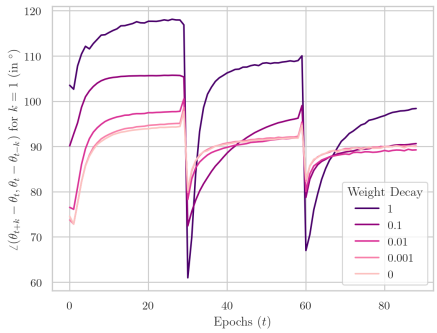

(c) $\angle(\theta_{t+k} - \theta_t, \theta_t - \theta_{t-k})$, for $k = 1$

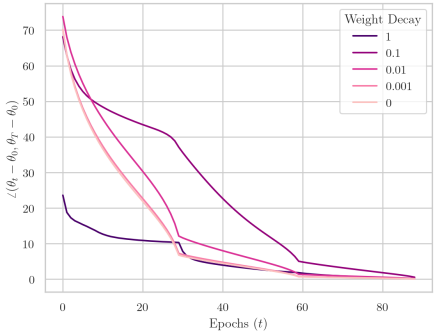

(d) $\angle(\theta_t - \theta_0, \theta_T - \theta_0)$

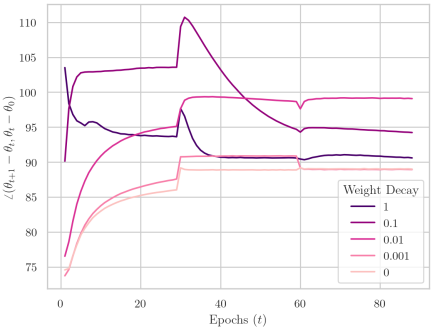

(e) $\angle(\theta_{t+1} - \theta_t, \theta_T - \theta_0)$

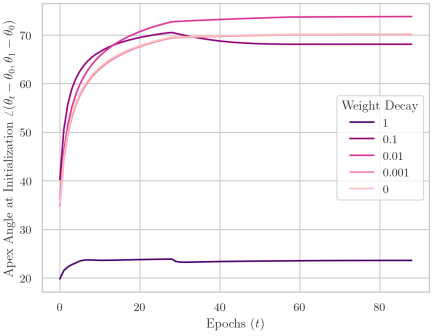

(f) Apex Angle at Initialization $\angle(\theta_t - \theta_0, \theta_1 - \theta_0)$

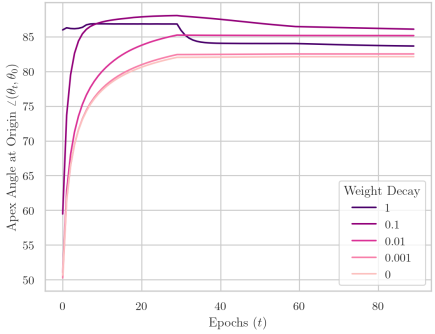

(g) Apex Angle at Origin $\angle(\theta_t, \theta_0)$

Figure 22. Angular measures of the Trajectory for ResNet50 trained on ImageNet

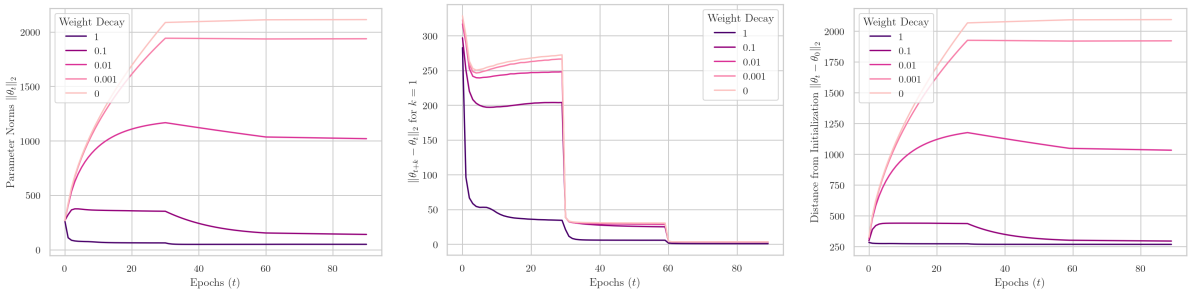

(a) $\|\theta_t\|_2$ (b) $\|\theta_{t+k} - \theta_t\|_2$ (c) $\|\theta_t - \theta_0\|_2$

Figure 23. Norm-based measures of the Trajectory for ResNet50 trained on ImageNet

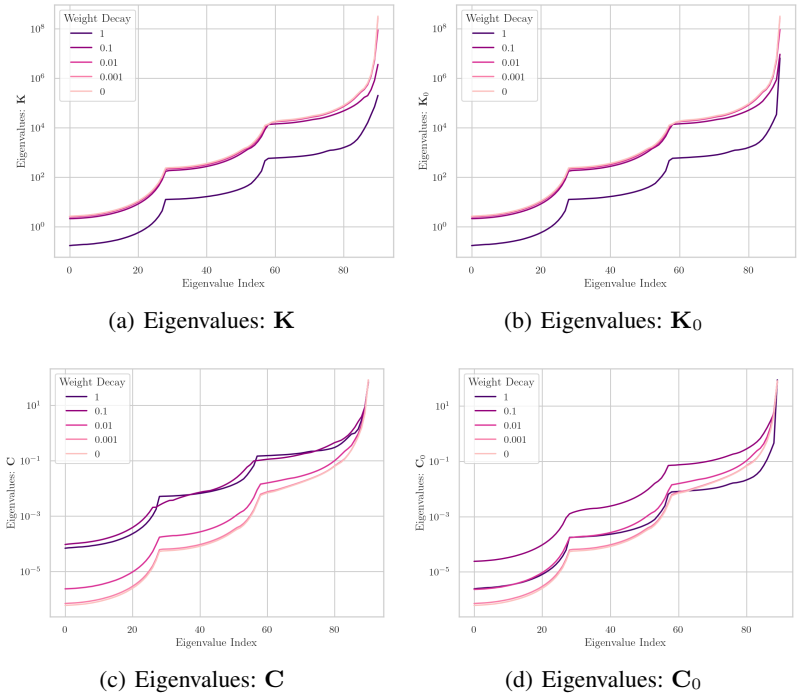

(a) Eigenvalues: $\mathbf{K}$ (b) Eigenvalues: $\mathbf{K}_0$

(c) Eigenvalues: $\mathbf{C}$ (d) Eigenvalues: $\mathbf{C}_0$

Figure 24. Spectral measures of the Trajectory for ResNet50 trained on ImageNet

C.4. ViT: Weight Decay, AdamW

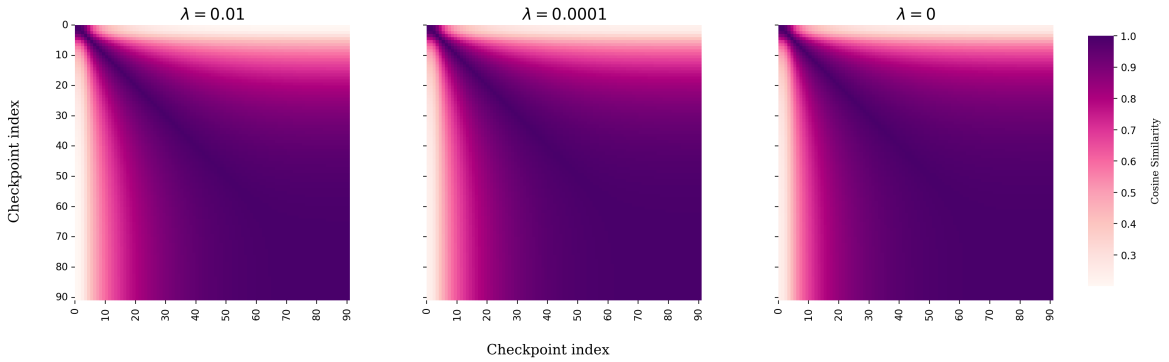

Figure 25. Trajectory Maps of ViT models across different amounts of weight decay

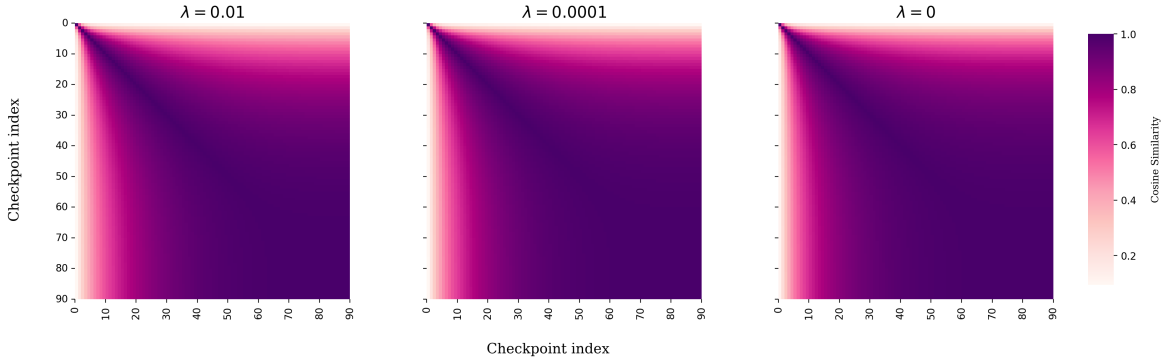

Figure 26. Relative Trajectory Maps, with respect to initialization, of ViT models across different amounts of weight decay

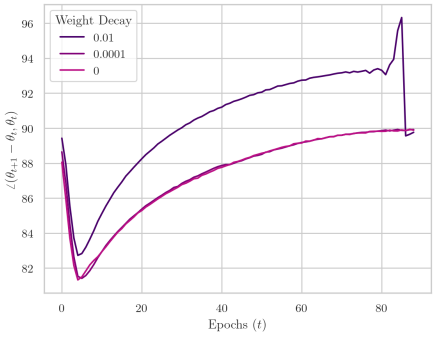

(a) $\angle(\theta_{t+1}-\theta_t,\theta_t)$

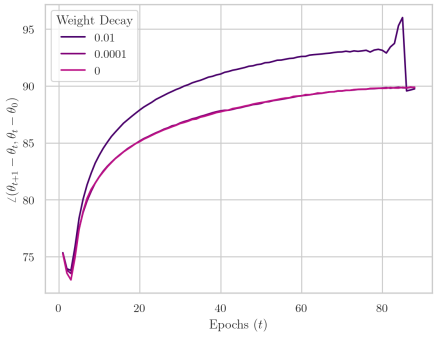

(b) $\angle(\theta_{t+1}-\theta_t,\theta_T-\theta_0)$

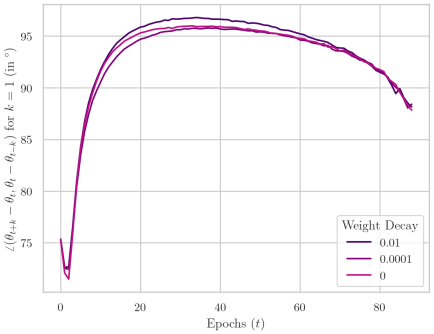

(c) $\angle(\theta_{t+k}-\theta_t,\theta_t-\theta_{t-k})$, for $k=1$

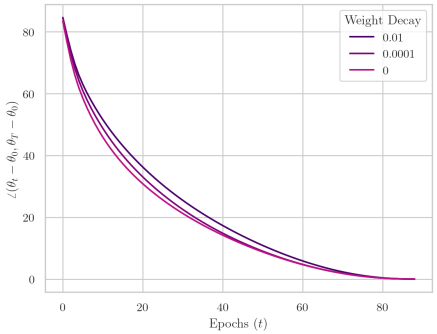

(d) $\angle(\theta_t-\theta_0,\theta_T-\theta_0)$

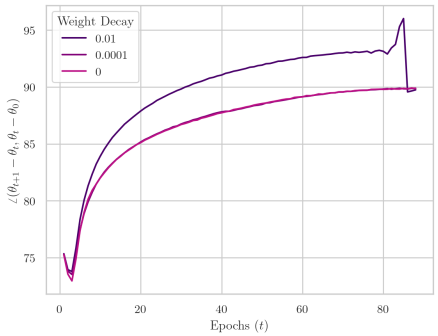

(e) $\angle(\theta_{t+1}-\theta_t,\theta_T-\theta_0)$

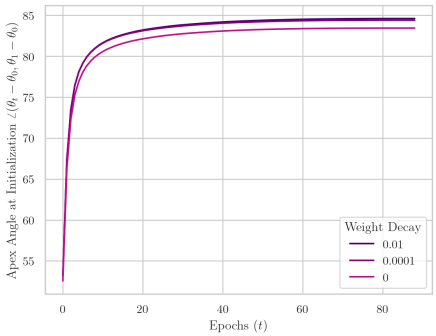

(f) Apex Angle at Initialization $\angle(\theta_t-\theta_0,\theta_1-\theta_0)$

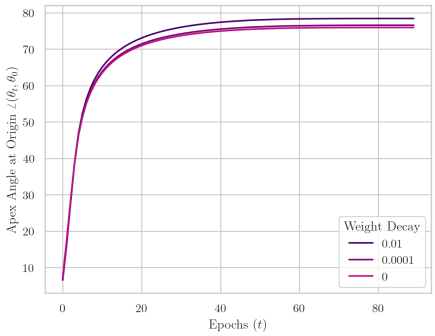

(g) Apex Angle at Origin $\angle(\theta_t,\theta_0)$

Figure 27. Angular measures of the Trajectory for ViT trained on the ImageNet dataset

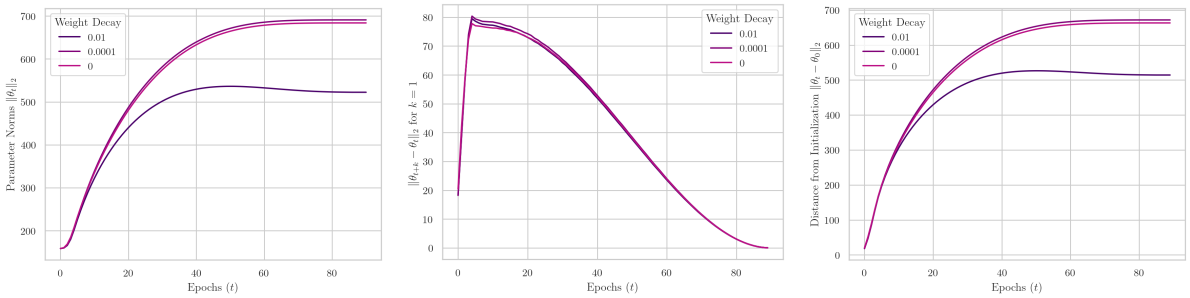

(a) $\|\theta_t\|_2$ (b) $\|\theta_{t+k} - \theta_t\|_2$ (c) $\|\theta_t - \theta_0\|_2$

Figure 28. Norm-based measures of the Trajectory for ViT trained on the ImageNet dataset

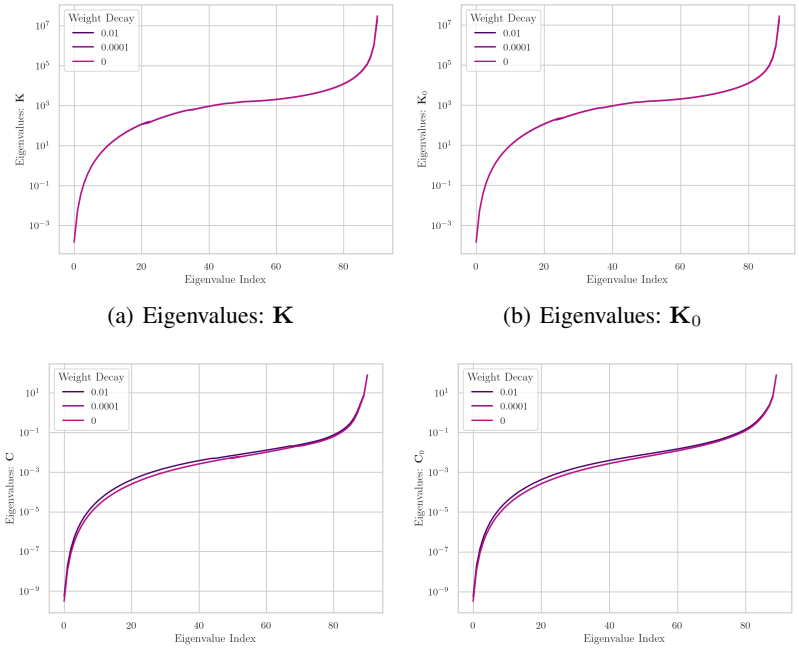

(a) Eigenvalues: $\mathbf{K}$ (b) Eigenvalues: $\mathbf{K}_0$

(c) Eigenvalues: $\mathbf{C}$ (d) Eigenvalues: $\mathbf{C}_0$

Figure 29. Spectral measures of the Trajectory for ViT trained on ImageNet

C.5. ResNet50: Sharpness Aware Minimization analysis

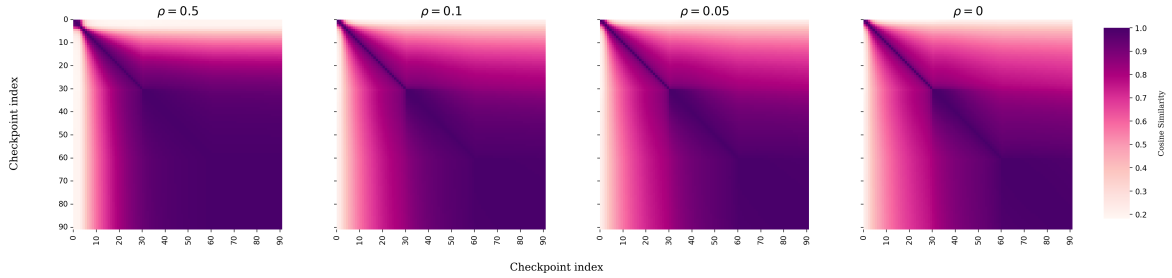

Figure 30. Trajectory Maps of ResNet50 models across different values of SAM regularization coefficient

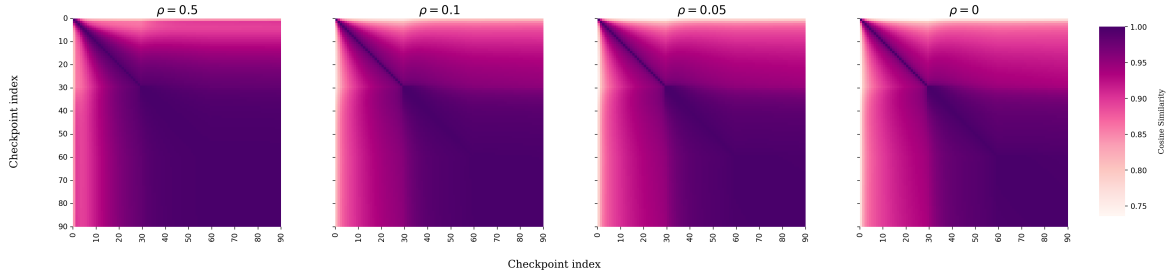

Figure 31. Relative Trajectory Maps, with respect to initialization, of ResNet50 models across different values of SAM regularization coefficient

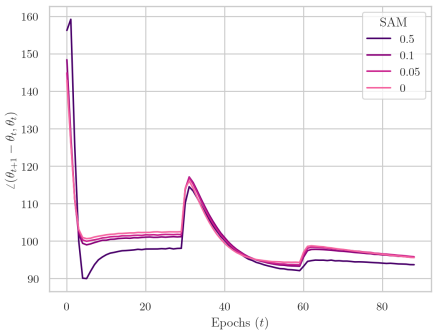

(a) $\angle(\theta_{t+1} - \theta_t, \theta_t)$

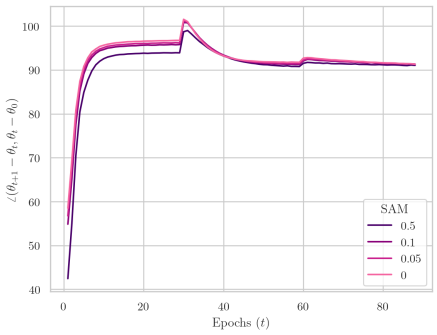

(b) $\angle(\theta_{t+1} - \theta_t, \theta_T - \theta_0)$

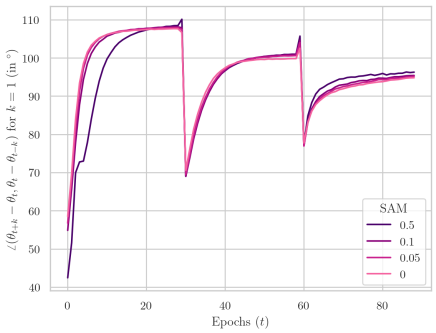

(c) $\angle(\theta_{t+k} - \theta_t, \theta_t - \theta_{t-k})$, for $k = 1$

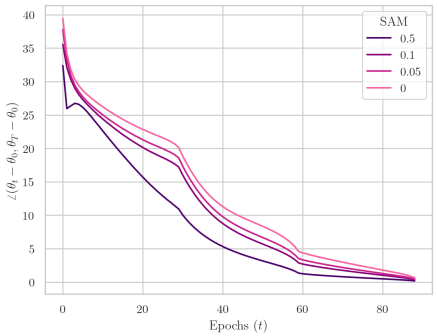

(d) $\angle(\theta_t - \theta_0, \theta_T - \theta_0)$

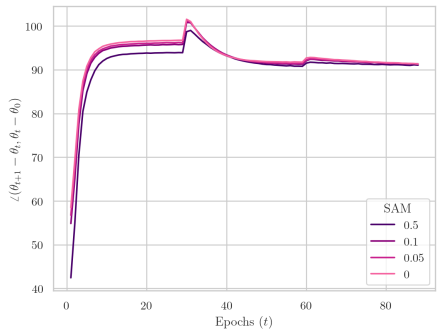

(e) $\angle(\theta_{t+1} - \theta_t, \theta_T - \theta_0)$

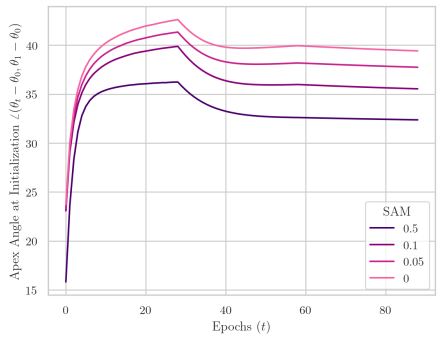

(f) Apex Angle at Initialization $\angle(\theta_t - \theta_0, \theta_1 - \theta_0)$

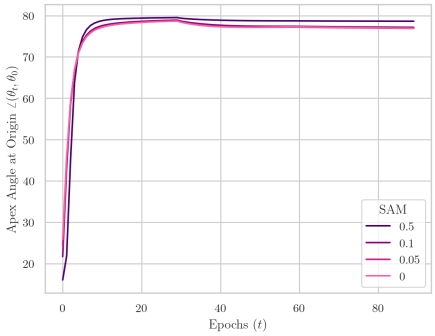

(g) Apex Angle at Origin $\angle(\theta_t, \theta_0)$

Figure 32. Angular measures of the Trajectory for ResNet50 trained on ImageNet

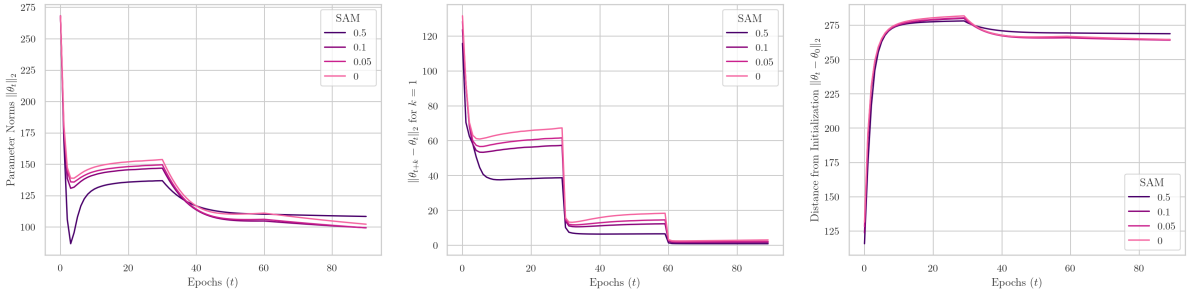

(a) $\|\theta_t\|_2$ (b) $\|\theta_{t+k} - \theta_t\|_2$ (c) $\|\theta_t - \theta_0\|_2$

Figure 33. Norm-based measures of the Trajectory for ResNet50 trained on ImageNet

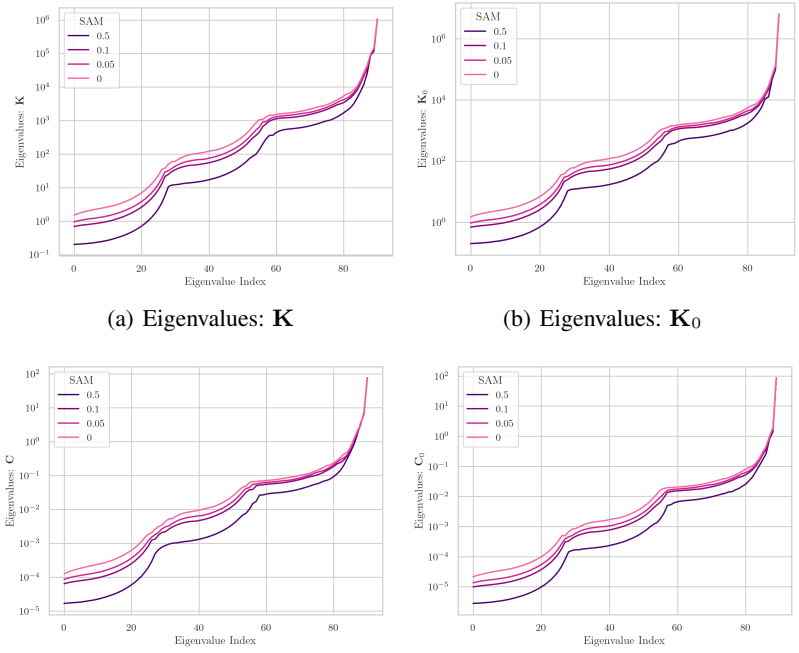

(a) Eigenvalues: $\mathbf{K}$ (b) Eigenvalues: $\mathbf{K}_0$

(c) Eigenvalues: $\mathbf{C}$ (d) Eigenvalues: $\mathbf{C}_0$

Figure 34. Spectral measures of the Trajectory for ResNet50 trained on ImageNet

C.6. ResNet50: Momentum Analysis, LR 0.1, WD 0.0001

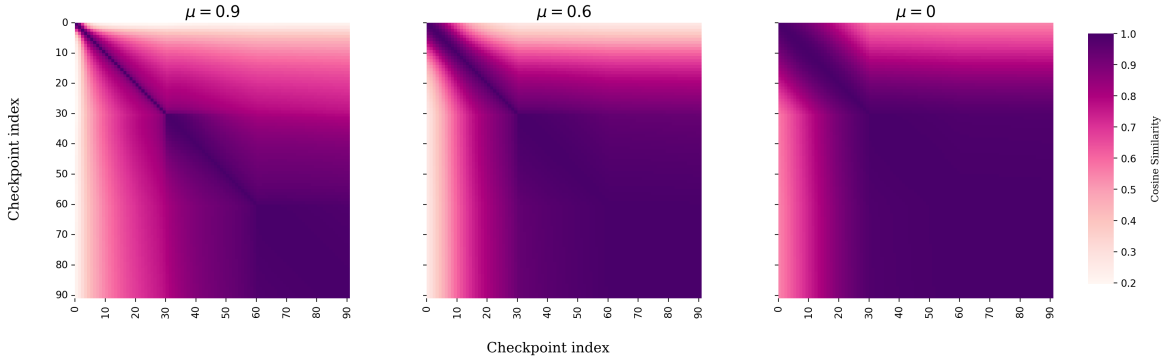

Figure 35. Trajectory Maps of ResNet50 models across different amounts of momentum

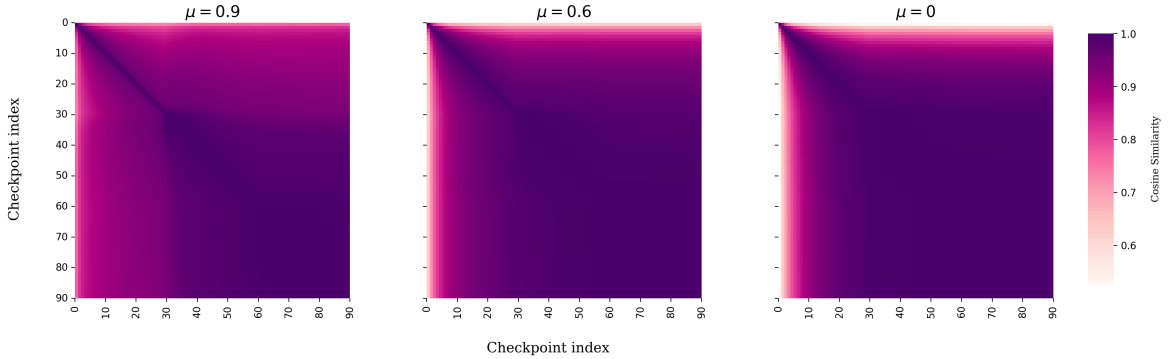

Figure 36. Relative Trajectory Maps, with respect to initialization, of ResNet50 models across different amounts of momentum

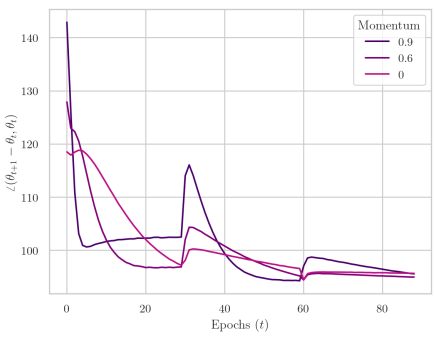

(a) $\angle(\theta_{t+1} - \theta_t, \theta_t)$

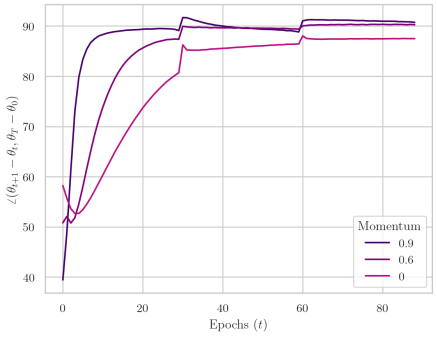

(b) $\angle(\theta_{t+1} - \theta_t, \theta_T - \theta_0)$

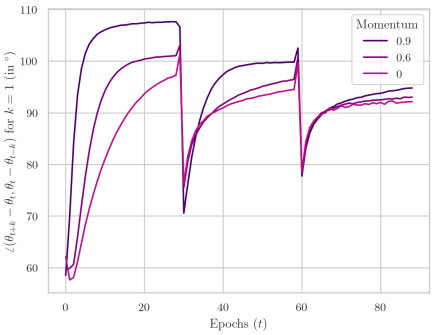

(c) $\angle(\theta_{t+k} - \theta_t, \theta_t - \theta_{t-k})$, for $k = 1$

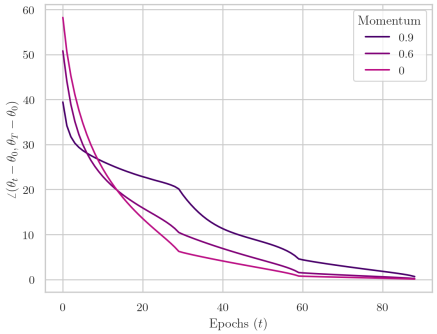

(d) $\angle(\theta_t - \theta_0, \theta_T - \theta_0)$

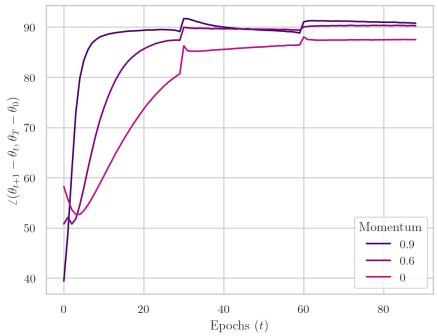

(e) $\angle(\theta_{t+1} - \theta_t, \theta_T - \theta_0)$

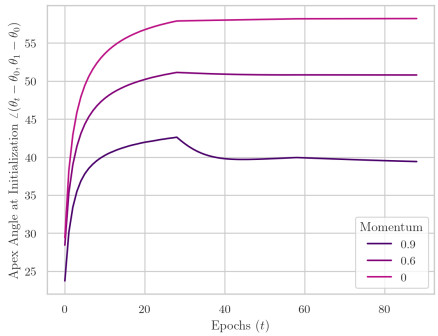

(f) Apex Angle at Initialization $\angle(\theta_t - \theta_0, \theta_1 - \theta_0)$

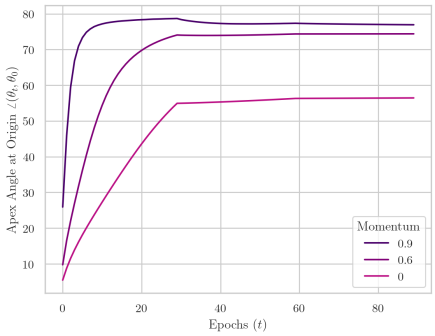

(g) Apex Angle at Origin $\angle(\theta_t, \theta_0)$

Figure 37. Angular measures of the Trajectory for ResNet50 trained on ImageNet

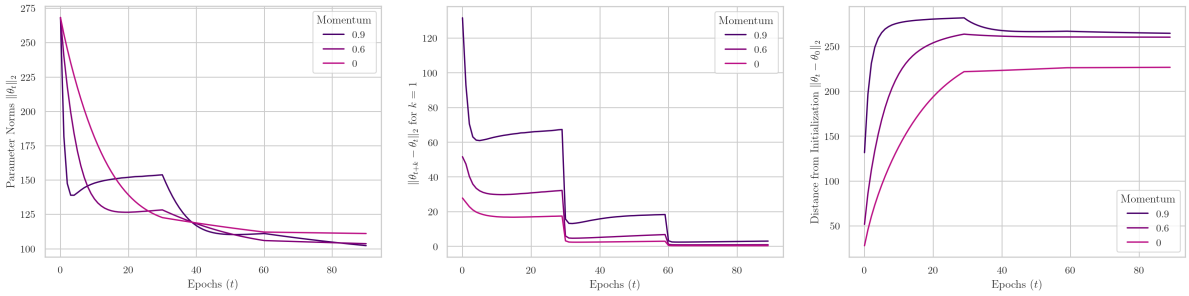

(a) $\|\theta_t\|_2$ (b) $\|\theta_{t+k} - \theta_t\|_2$ (c) $\|\theta_t - \theta_0\|_2$

Figure 38. Norm-based measures of the Trajectory for ResNet50 trained on ImageNet

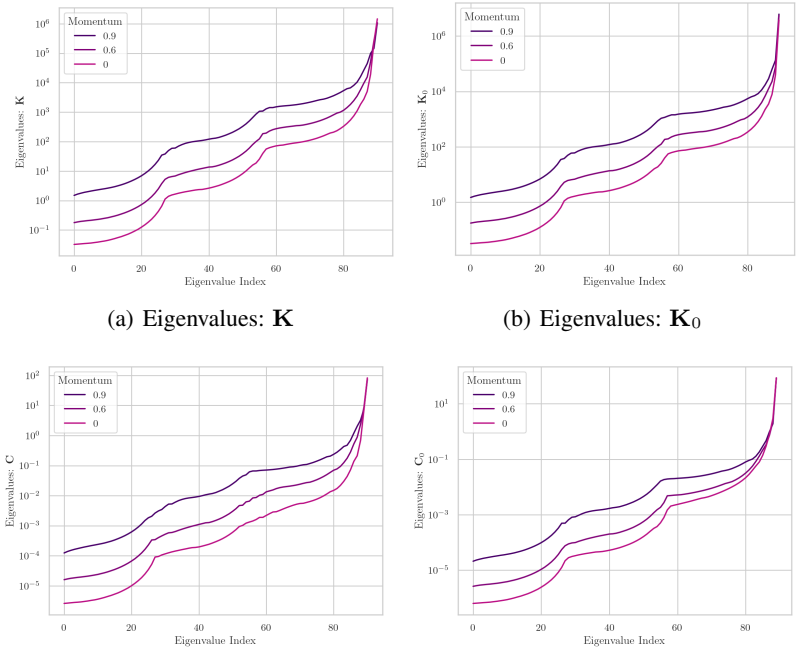

(a) Eigenvalues: $\mathbf{K}$ (b) Eigenvalues: $\mathbf{K}_0$

(c) Eigenvalues: $\mathbf{C}$ (d) Eigenvalues: $\mathbf{C}_0$

Figure 39. Spectral measures of the Trajectory for ResNet50 trained on ImageNet

C.7. VGG: Momentum Analysis, LR 0.1, WD 0.0001

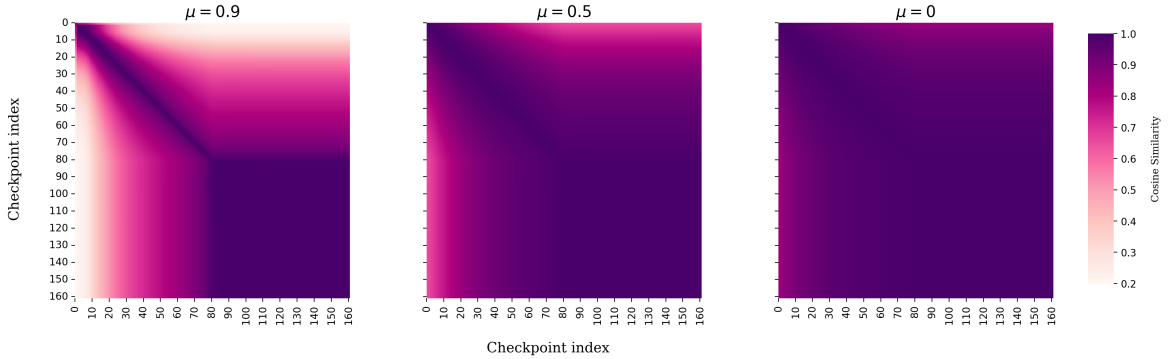

Figure 40. Trajectory Maps of VGG16 models across different amounts of momentum

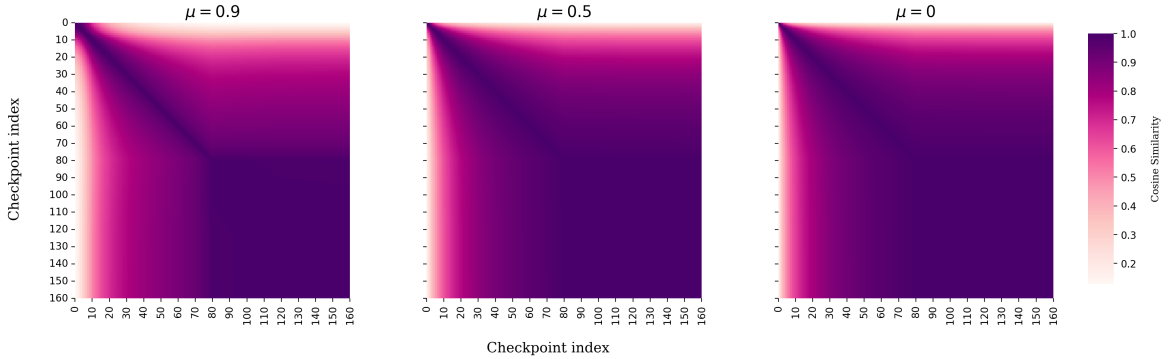

Figure 41. Relative Trajectory Maps, with respect to initialization, of VGG16 models across different amounts of momentum

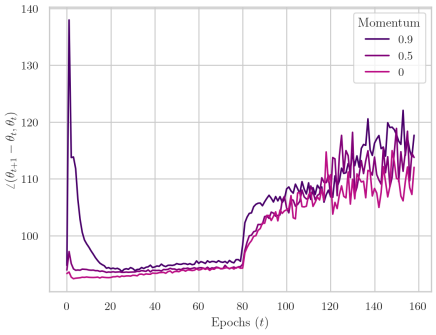

(a) $\angle(\theta_{t+1} - \theta_t, \theta_t)$

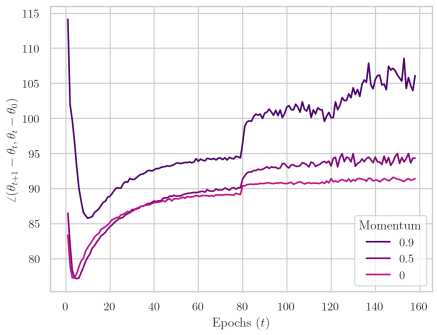

(b) $\angle(\theta_{t+1} - \theta_t, \theta_T - \theta_0)$

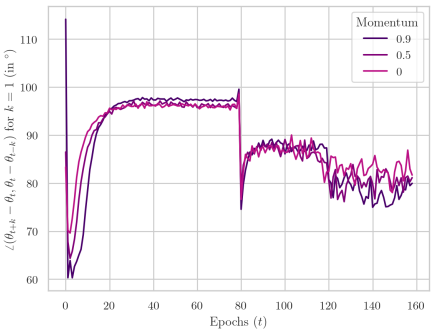

(c) $\angle(\theta_{t+k} - \theta_t, \theta_t - \theta_{t-k})$, for $k = 1$

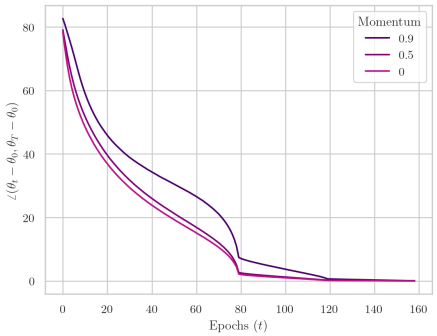

(d) $\angle(\theta_t - \theta_0, \theta_T - \theta_0)$

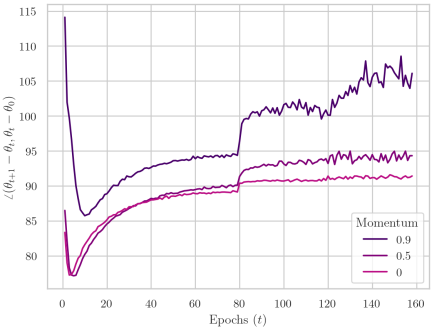

(e) $\angle(\theta_{t+1} - \theta_t, \theta_T - \theta_0)$

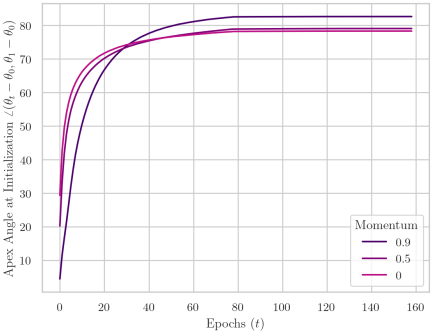

(f) Apex Angle at Initialization $\angle(\theta_t - \theta_0, \theta_1 - \theta_0)$

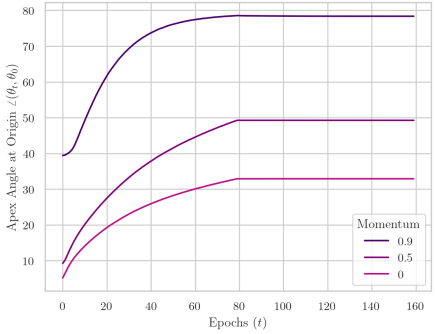

(g) Apex Angle at Origin $\angle(\theta_t, \theta_0)$

Figure 42. Angular measures of the Trajectory for VGG16 models trained on CIFAR10.

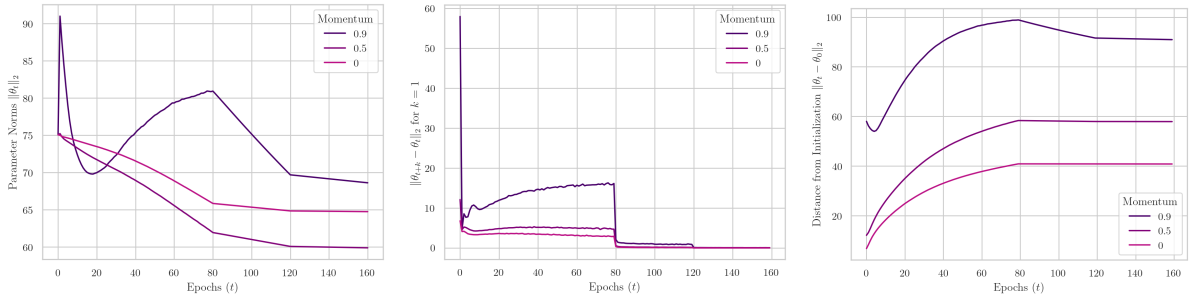

(a) $\|\theta_t\|_2$ (b) $\|\theta_{t+k} - \theta_t\|_2$ (c) $\|\theta_t - \theta_0\|_2$

Figure 43. Norm-based measures of the Trajectory for VGG16 models trained on CIFAR10.

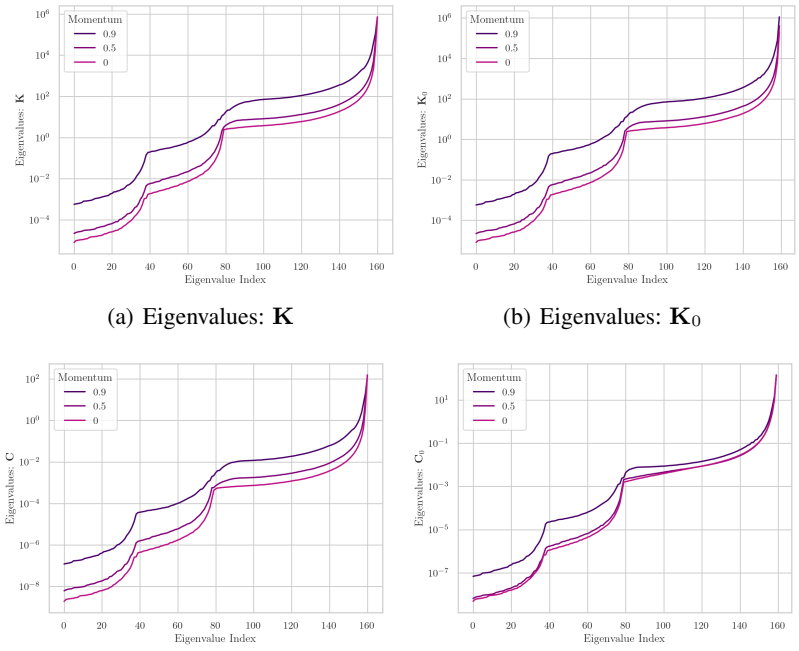

(a) Eigenvalues: $\mathbf{K}$ (b) Eigenvalues: $\mathbf{K}_0$

(c) Eigenvalues: $\mathbf{C}$ (d) Eigenvalues: $\mathbf{C}_0$

Figure 44. Spectral measures of the Trajectory for VGG16 models trained on CIFAR10.

C.8. VGG: Momentum Analysis, LR 0.1, WD 0

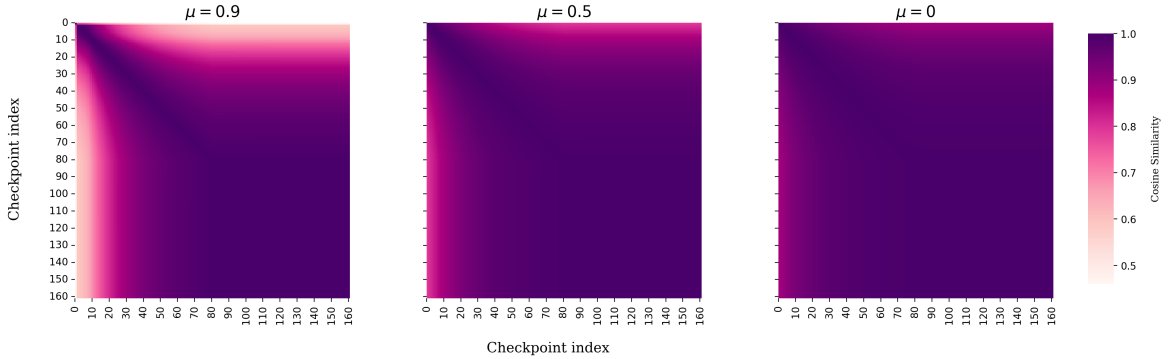

Figure 45. Trajectory Maps of VGG16 models across different amounts of momentum

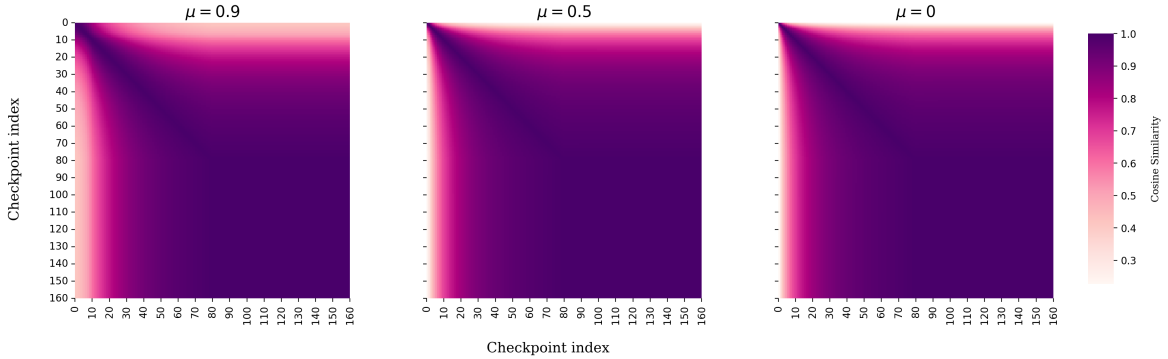

Figure 46. Relative Trajectory Maps, with respect to initialization, of VGG16 models across different amounts of momentum

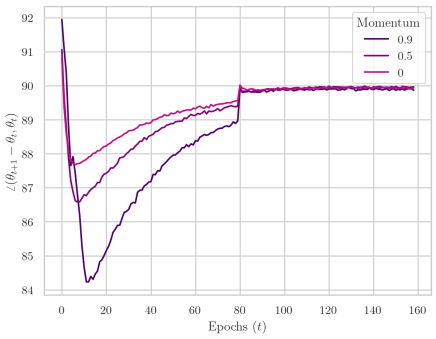

(a) $\angle(\theta_{t+1}-\theta_t,\theta_t)$

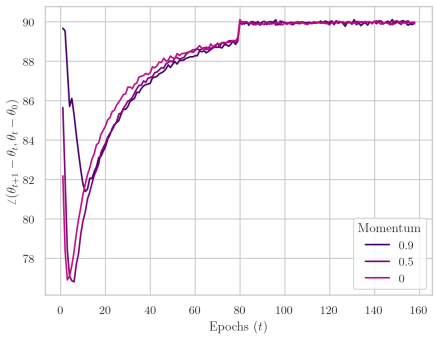

(b) $\angle(\theta_{t+1}-\theta_t,\theta_T-\theta_0)$

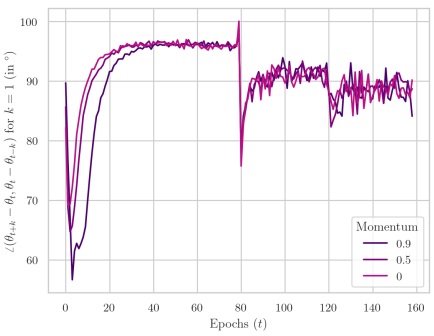

(c) $\angle(\theta_{t+k}-\theta_t,\theta_t-\theta_{t-k})$, for $k=1$

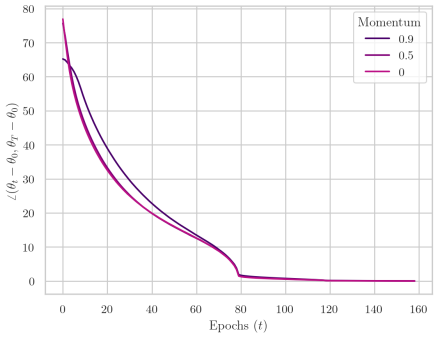

(d) $\angle(\theta_t-\theta_0,\theta_T-\theta_0)$

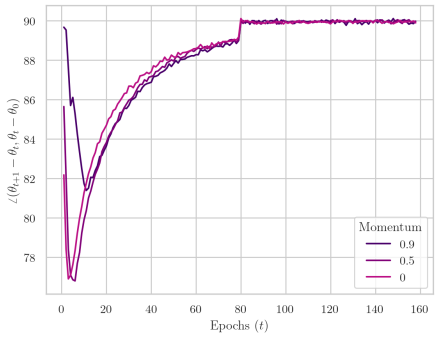

(e) $\angle(\theta_{t+1}-\theta_t,\theta_T-\theta_0)$

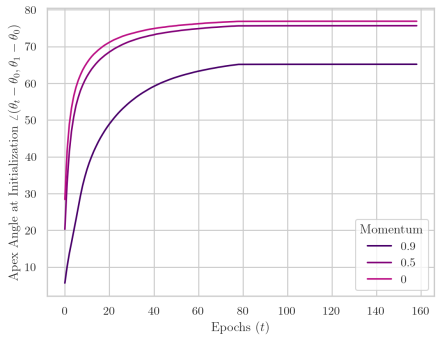

(f) Apex Angle at Initialization $\angle(\theta_t-\theta_0,\theta_1-\theta_0)$

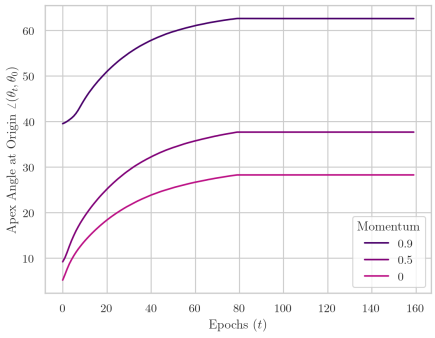

(g) Apex Angle at Origin $\angle(\theta_t,\theta_0)$

Figure 47. Angular measures of the Trajectory for VGG16 models trained on CIFAR10.

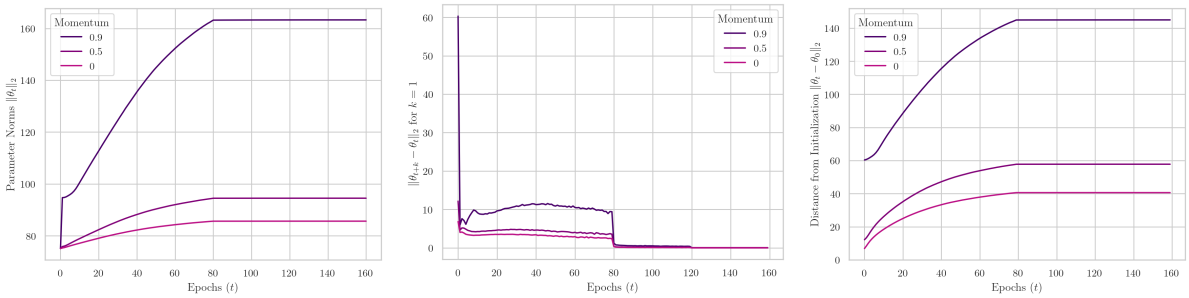

(a) $\|\theta_t\|_2$ (b) $\|\theta_{t+k} - \theta_t\|_2$ (c) $\|\theta_t - \theta_0\|_2$

Figure 48. Norm-based measures of the Trajectory for VGG16 models trained on CIFAR10.

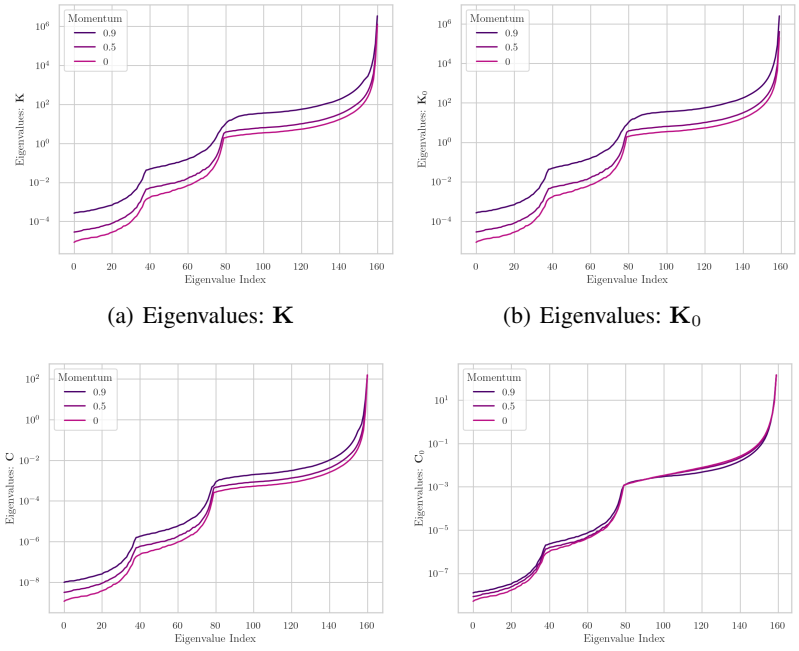

(a) Eigenvalues: $\mathbf{K}$ (b) Eigenvalues: $\mathbf{K}_0$

(c) Eigenvalues: $\mathbf{C}$ (d) Eigenvalues: $\mathbf{C}_0$

Figure 49. Spectral measures of the Trajectory for VGG16 models trained on CIFAR10.

C.9. VGG: Momentum Analysis, LR 0.01, WD 0.0001

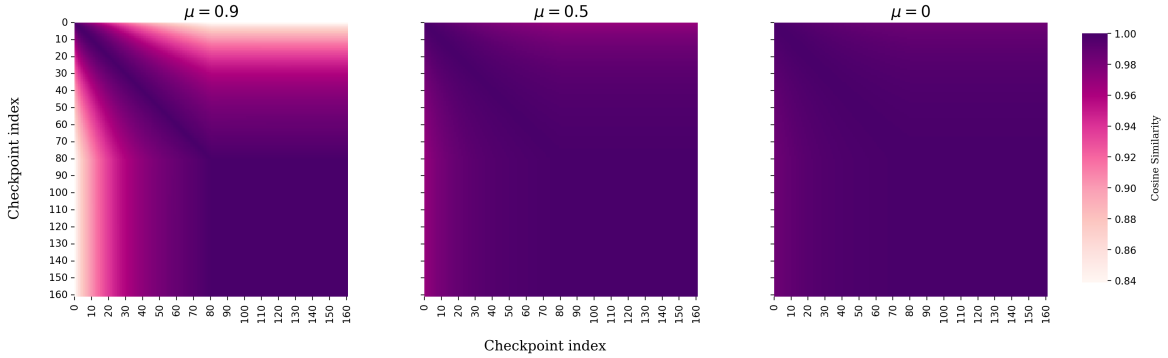

Figure 50. Trajectory Maps of VGG16 models across different amounts of momentum

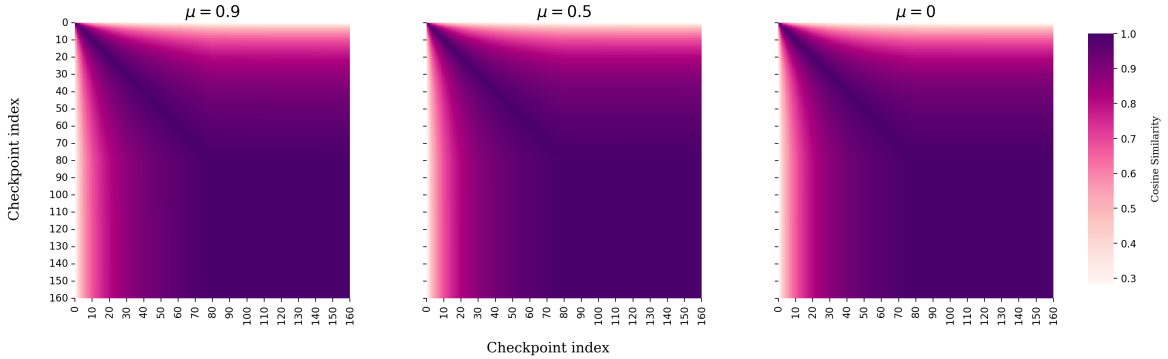

Figure 51. Relative Trajectory Maps, with respect to initialization, of VGG16 models across different amounts of momentum

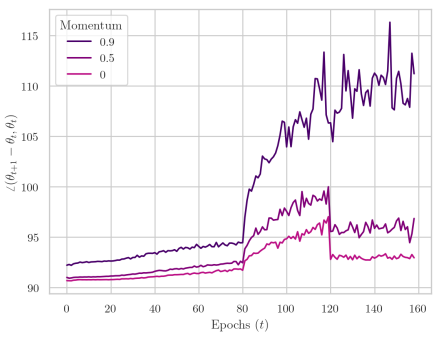

(a) $\angle(\theta_{t+1} - \theta_t, \theta_t)$

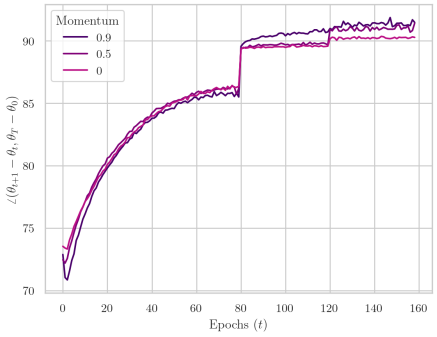

(b) $\angle(\theta_{t+1} - \theta_t, \theta_T - \theta_0)$

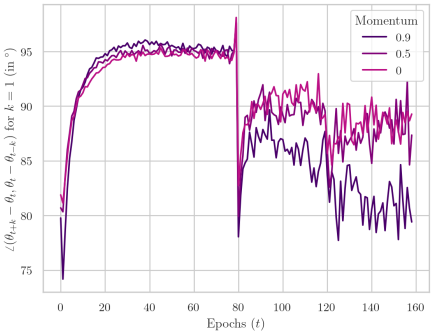

(c) $\angle(\theta_{t+k} - \theta_t, \theta_t - \theta_{t-k})$, for $k = 1$

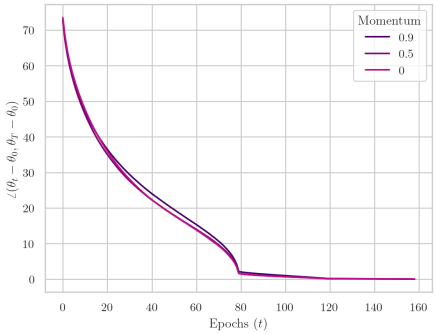

(d) $\angle(\theta_t - \theta_0, \theta_T - \theta_0)$

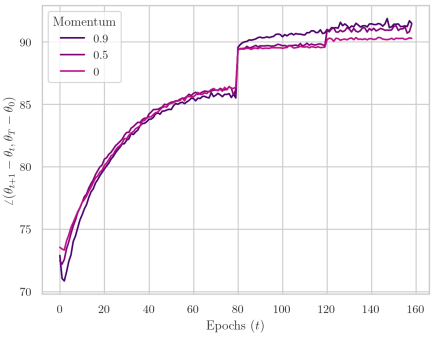

(e) $\angle(\theta_{t+1} - \theta_t, \theta_T - \theta_0)$

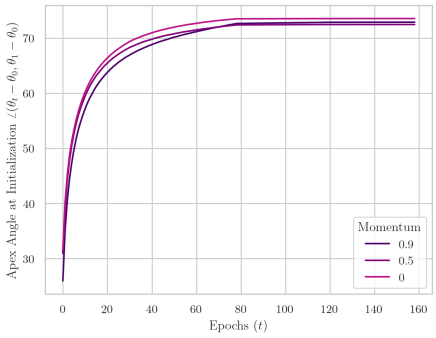

(f) Apex Angle at Initialization $\angle(\theta_t - \theta_0, \theta_1 - \theta_0)$

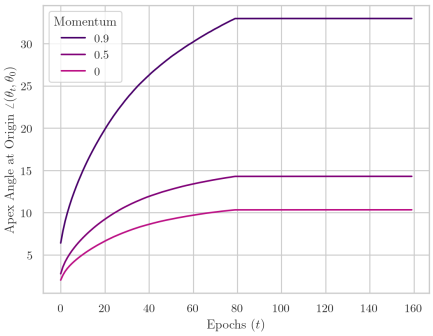

(g) Apex Angle at Origin $\angle(\theta_t, \theta_0)$

Figure 52. Angular measures of the Trajectory for VGG16 models trained on CIFAR10.

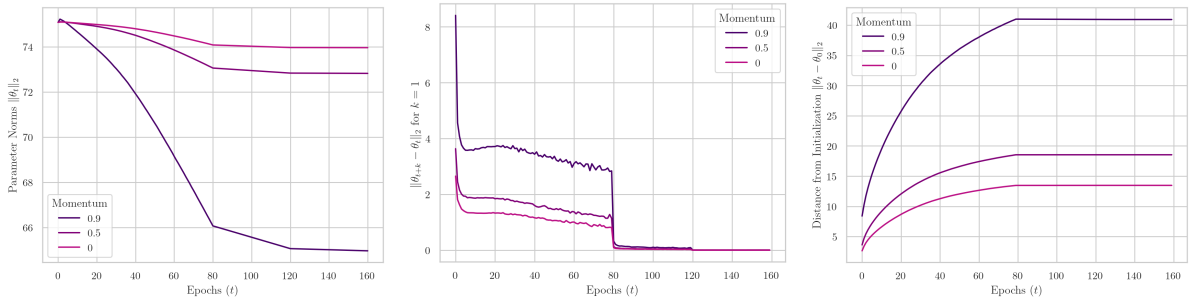

(a) $\|\theta_t\|_2$ (b) $\|\theta_{t+k} - \theta_t\|_2$ (c) $\|\theta_t - \theta_0\|_2$

Figure 53. Norm-based measures of the Trajectory for VGG16 models trained on CIFAR10.

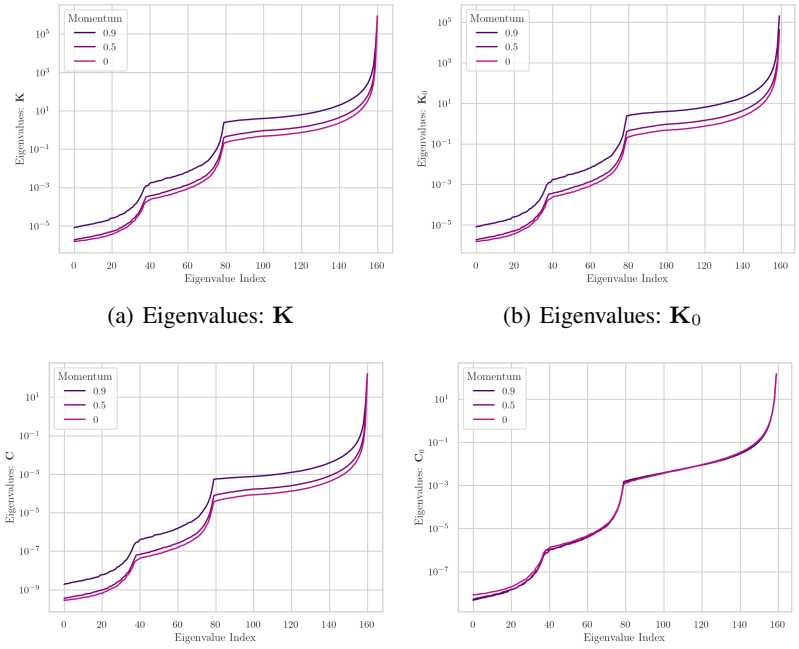

(a) Eigenvalues: $\mathbf{K}$ (b) Eigenvalues: $\mathbf{K}_0$

(c) Eigenvalues: $\mathbf{C}$ (d) Eigenvalues: $\mathbf{C}_0$

Figure 54. Spectral measures of the Trajectory for VGG16 models trained on CIFAR10.

C.10. VGG: Momentum Analysis, LR 0.01, WD 0

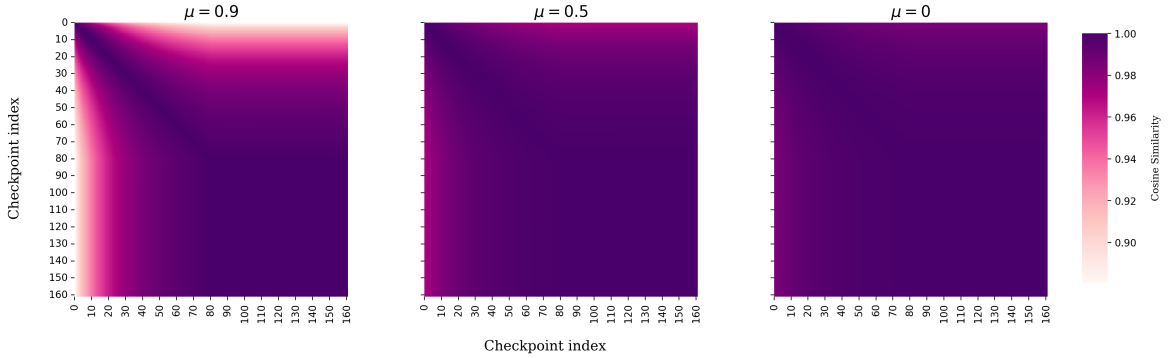

Figure 55. Trajectory Maps of VGG16 models across different amounts of momentum

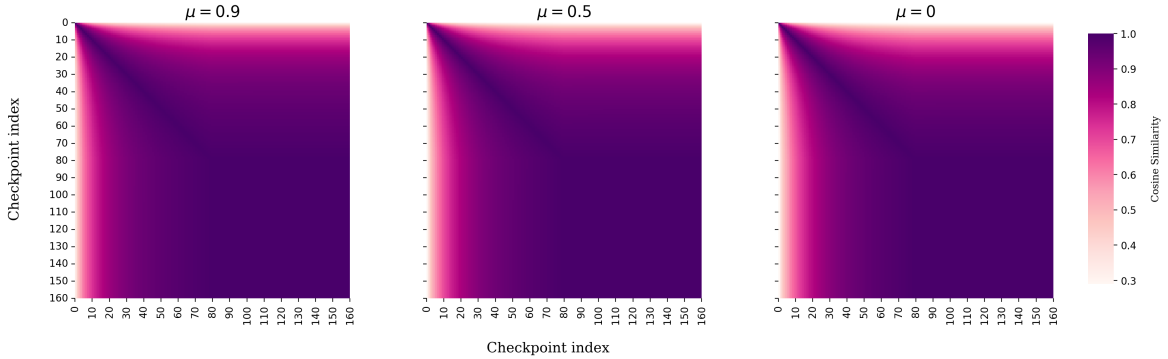

Figure 56. Relative Trajectory Maps, with respect to initialization, of VGG16 models across different amounts of momentum

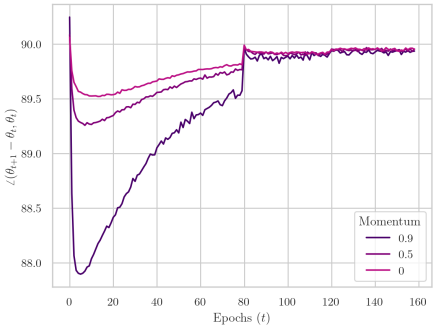

(a) $\angle(\theta_{t+1} - \theta_t, \theta_t)$

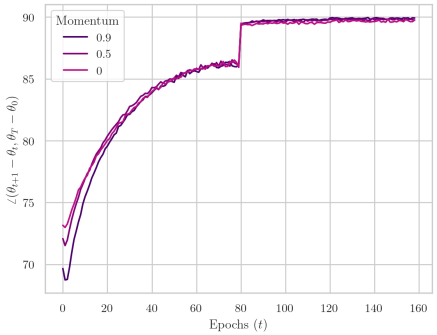

(b) $\angle(\theta_{t+1} - \theta_t, \theta_T - \theta_0)$

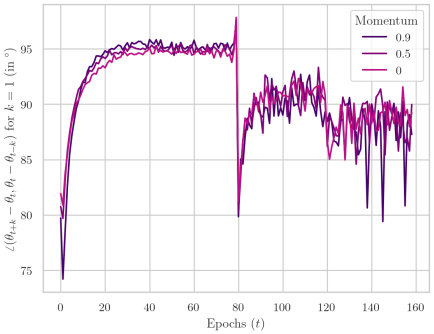

(c) $\angle(\theta_{t+k} - \theta_t, \theta_t - \theta_{t-k})$, for $k = 1$

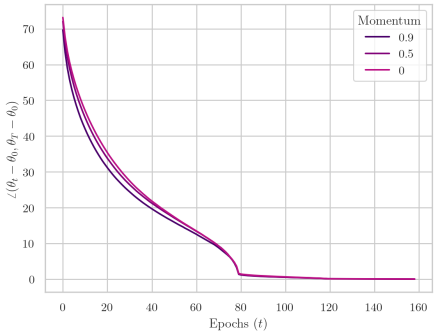

(d) $\angle(\theta_t - \theta_0, \theta_T - \theta_0)$

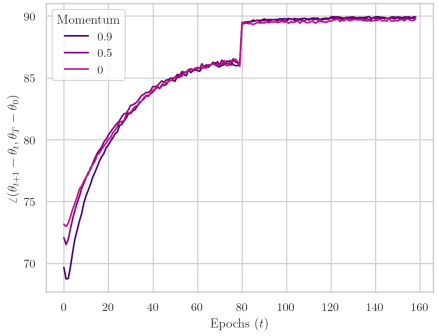

(e) $\angle(\theta_{t+1} - \theta_t, \theta_T - \theta_0)$

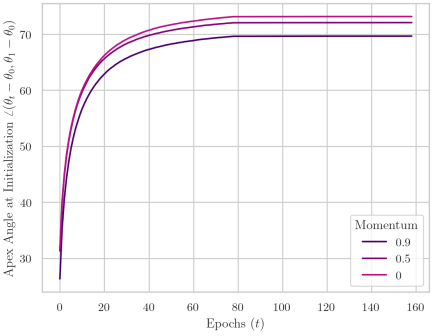

(f) Apex Angle at Initialization $\angle(\theta_t - \theta_0, \theta_1 - \theta_0)$

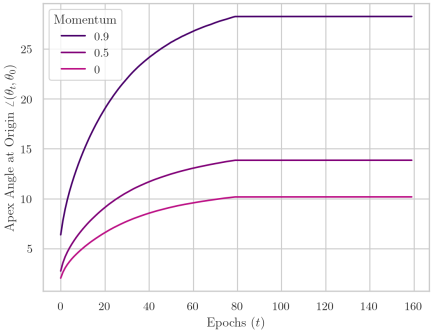

(g) Apex Angle at Origin $\angle(\theta_t, \theta_0)$

Figure 57. Angular measures of the Trajectory for VGG16 models trained on CIFAR10.

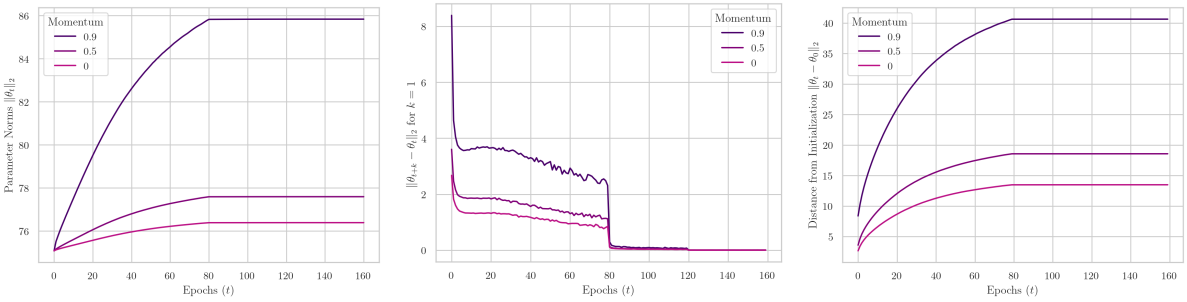

(a) $\|\theta_t\|_2$ (b) $\|\theta_{t+k} - \theta_t\|_2$ (c) $\|\theta_t - \theta_0\|_2$

Figure 58. Norm-based measures of the Trajectory for VGG16 models trained on CIFAR10.

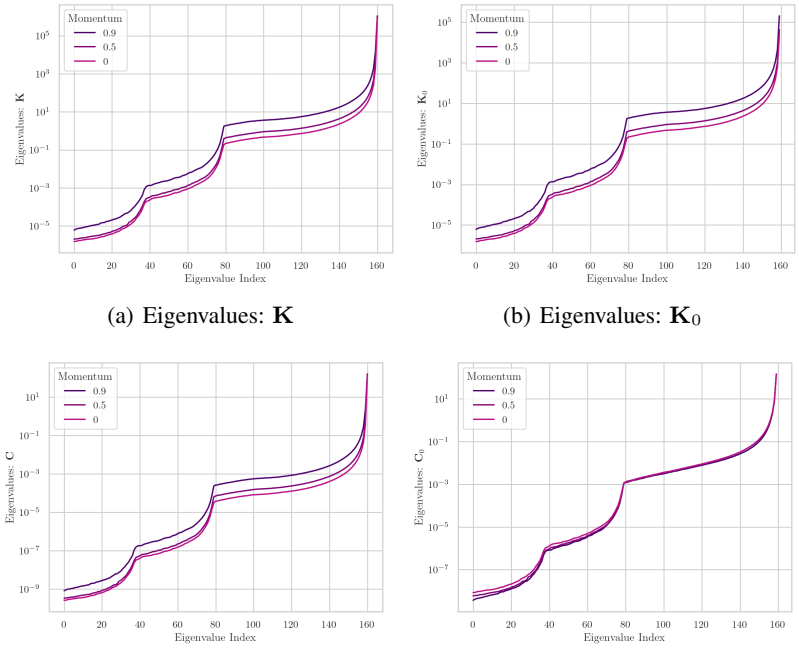

(a) Eigenvalues: $\mathbf{K}$ (b) Eigenvalues: $\mathbf{K}_0$

(c) Eigenvalues: $\mathbf{C}$ (d) Eigenvalues: $\mathbf{C}_0$

Figure 59. Spectral measures of the Trajectory for VGG16 models trained on CIFAR10.

C.11. VGG16 Batch Size Analysis

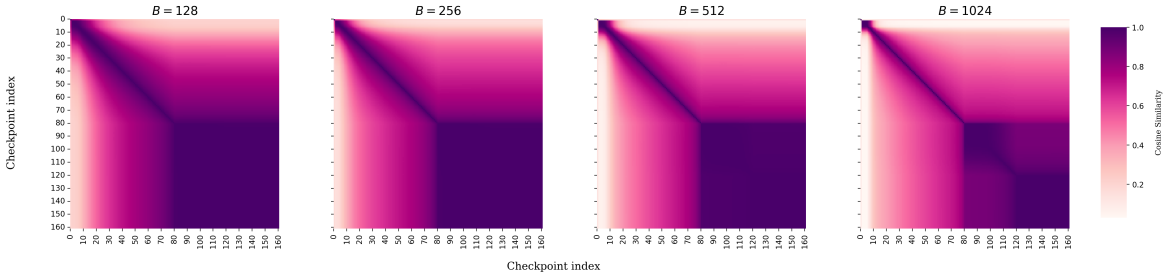

Figure 60. Trajectory Maps of VGG16 models across different batch sizes

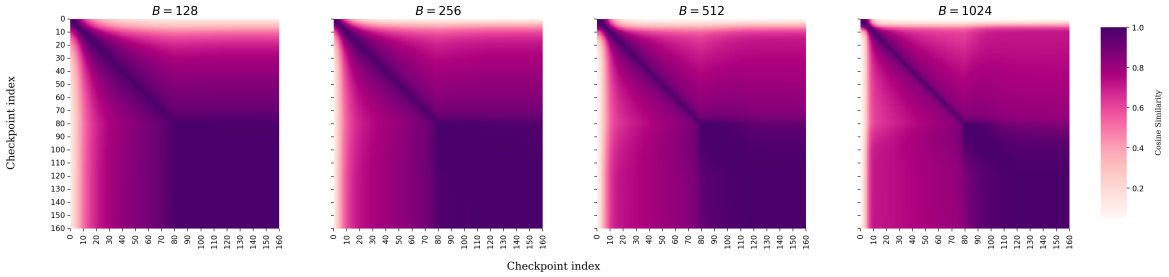

Figure 61. Relative Trajectory Maps, with respect to initialization, of VGG16 models across different batch sizes

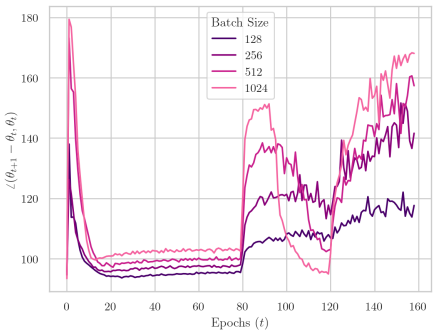

(a) $\angle(\theta_{t+1}-\theta_t,\theta_t)$

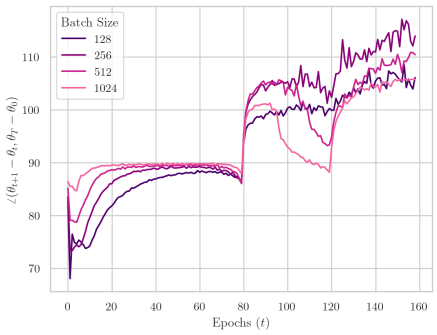

(b) $\angle(\theta_{t+1}-\theta_t,\theta_T-\theta_0)$

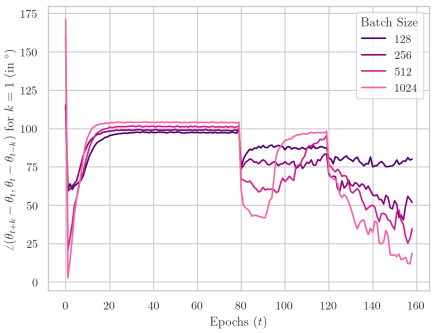

(c) $\angle(\theta_{t+k}-\theta_t,\theta_t-\theta_{t-k})$, for $k=1$

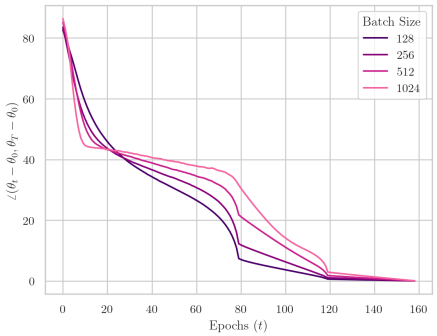

(d) $\angle(\theta_t-\theta_0,\theta_T-\theta_0)$

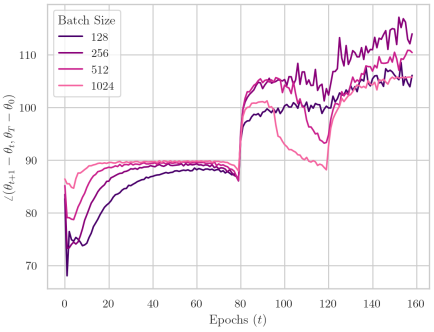

(e) $\angle(\theta_{t+1}-\theta_t,\theta_T-\theta_0)$

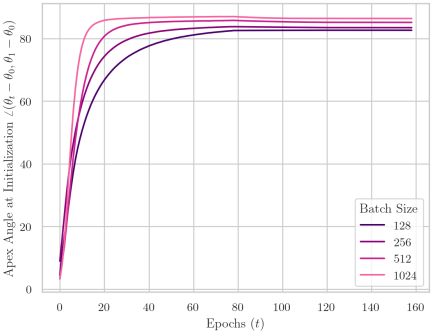

(f) Apex Angle at Initialization $\angle(\theta_t-\theta_0,\theta_1-\theta_0)$

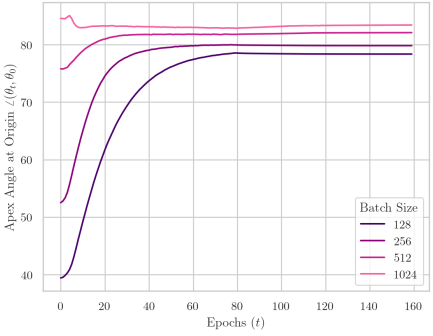

(g) Apex Angle at Origin $\angle(\theta_t,\theta_0)$

Figure 62. Angular measures of the Trajectory for VGG16 models trained on CIFAR10.

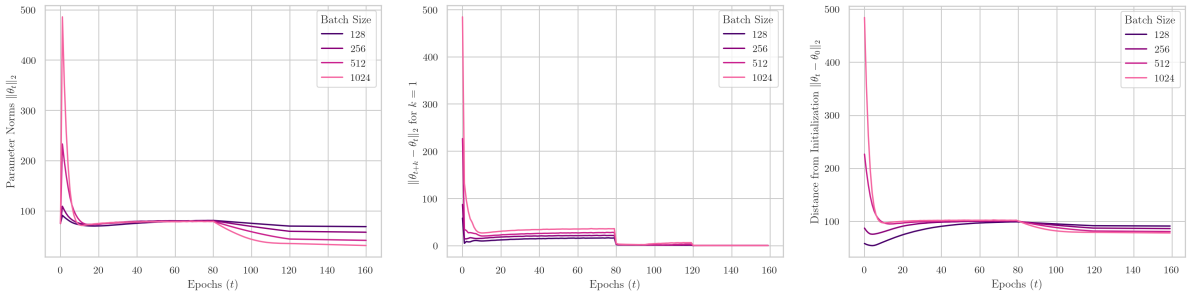

(a) $\|\theta_t\|_2$ (b) $\|\theta_{t+k} - \theta_t\|_2$ (c) $\|\theta_t - \theta_0\|_2$

Figure 63. Norm-based measures of the Trajectory for VGG16 models trained on CIFAR10.

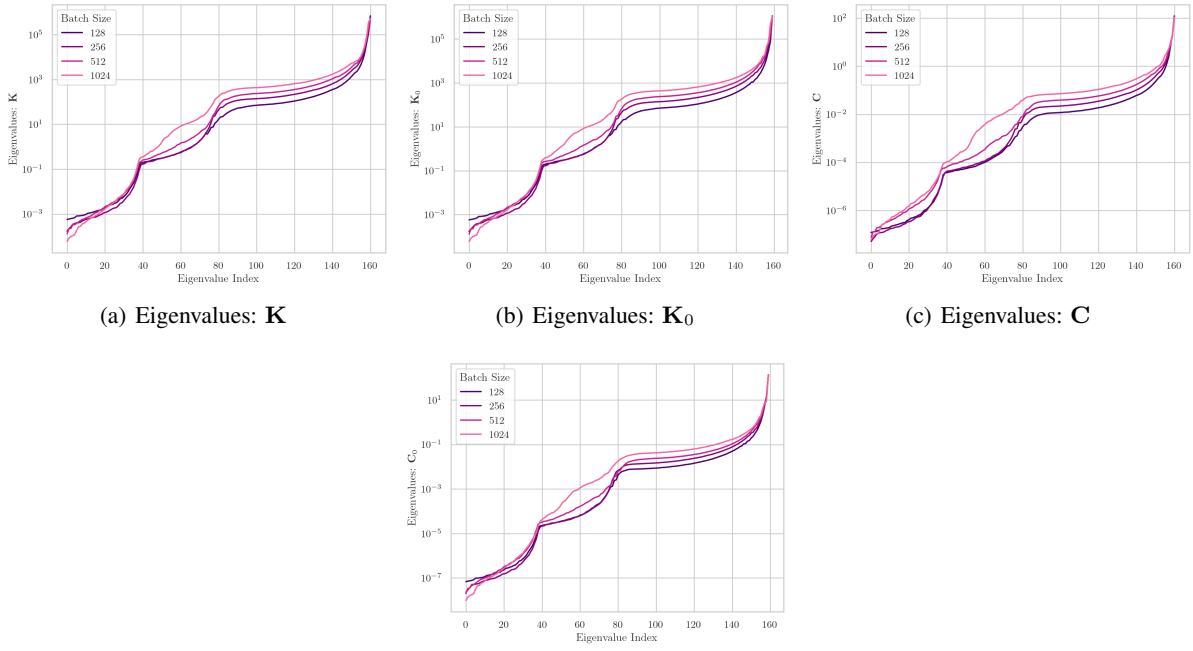

(a) Eigenvalues: $\mathbf{K}$ (b) Eigenvalues: $\mathbf{K}_0$ (c) Eigenvalues: $\mathbf{C}$

(d) Eigenvalues: $\mathbf{C}_0$

Figure 64. Spectral measures of the Trajectory for VGG16 models trained on CIFAR10.

D. GPT-NeoX Trajectory Analysis

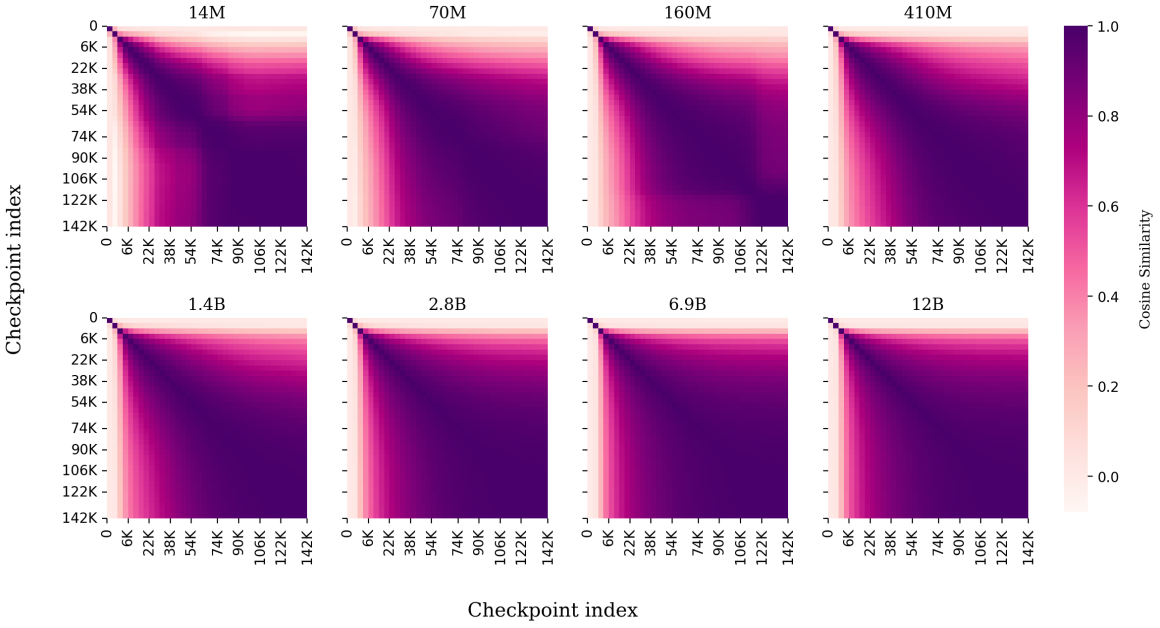

Figure 65. Relative Trajectory Maps, with respect to initialization, of Pythia GPT-NeoX models across two orders of model scales.

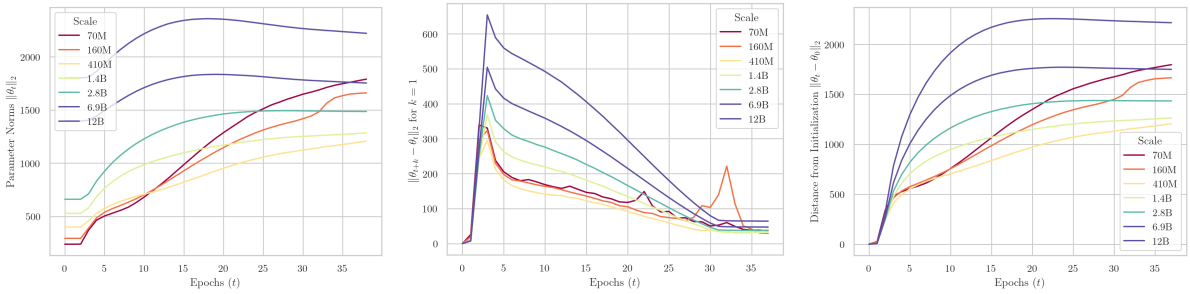

(a) $\|\theta_t\|_2$ (b) $\|\theta_{t+k} - \theta_t\|_2$ (c) $\|\theta_t - \theta_0\|_2$

Figure 66. Norm-based measures of the Trajectory for GPT-NeoX trained on the Pile dataset

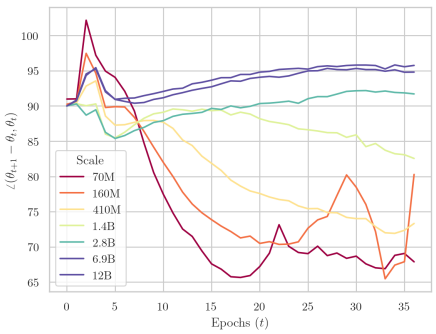

(a) $\angle(\theta_{t+1} - \theta_t, \theta_t)$

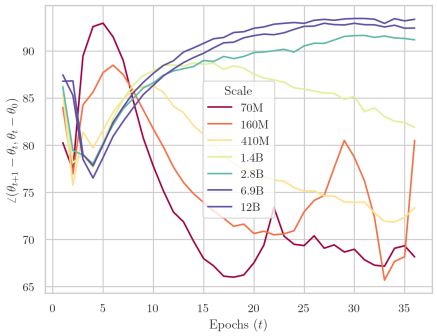

(b) $\angle(\theta_{t+1} - \theta_t, \theta_T - \theta_0)$

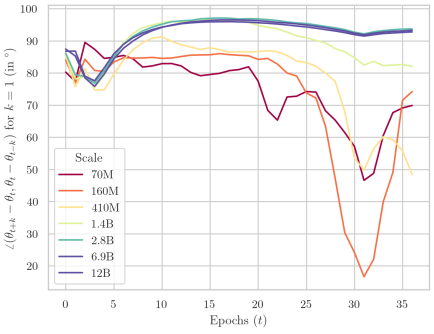

(c) $\angle(\theta_{t+k} - \theta_t, \theta_t - \theta_{t-k})$, for $k = 1$

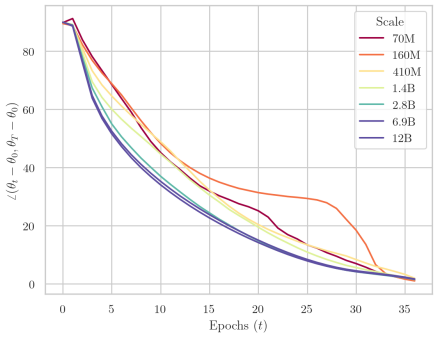

(d) $\angle(\theta_t - \theta_0, \theta_T - \theta_0)$

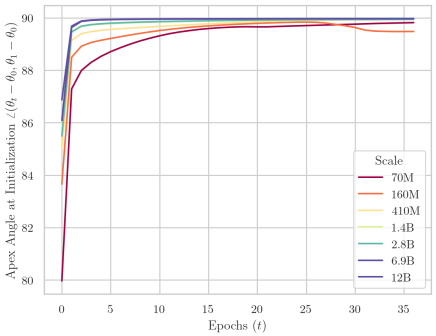

(e) Apex Angle at Initialization $\angle(\theta_t - \theta_0, \theta_1 - \theta_0)$

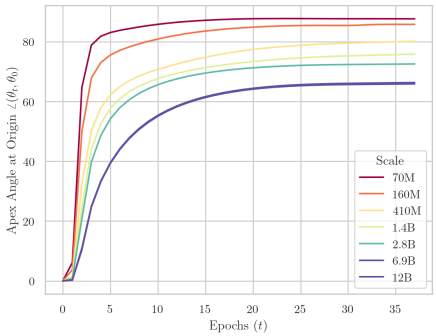

(f) Apex Angle at Origin $\angle(\theta_t, \theta_0)$

Figure 67. Angular measures of the Trajectory for GPT-NeoX trained on the Pile dataset

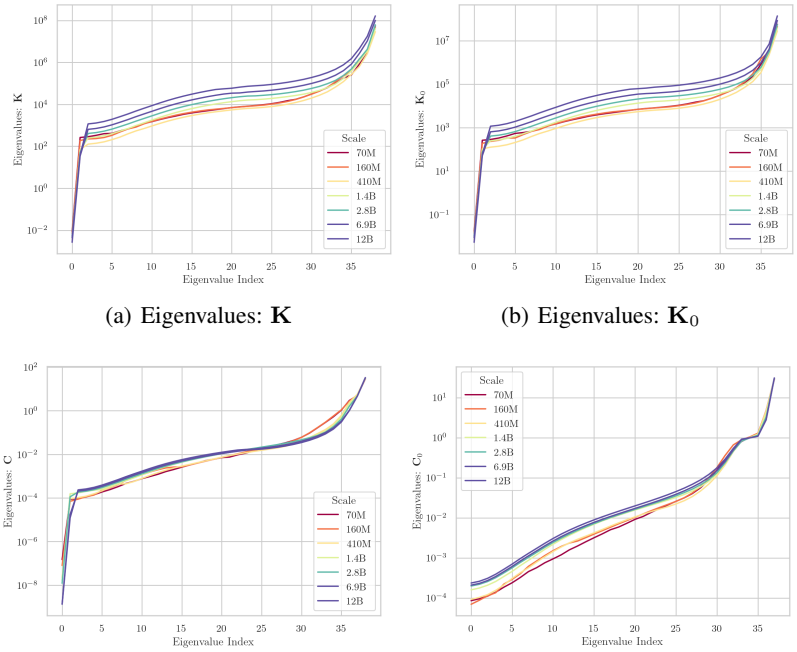

(a) Eigenvalues: $\mathbf{K}$ (b) Eigenvalues: $\mathbf{K}_0$

(c) Eigenvalues: $\mathbf{C}$ (d) Eigenvalues: $\mathbf{C}_0$

Figure 68. Spectral measures of the Trajectory for GPT-NeoX trained on the Pile dataset

E. Layerwise-Trajectory Maps

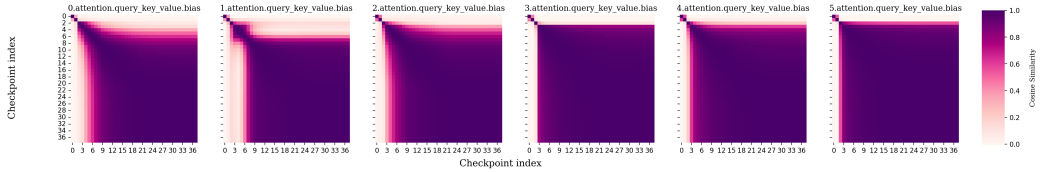

(a) query-key-value, bias

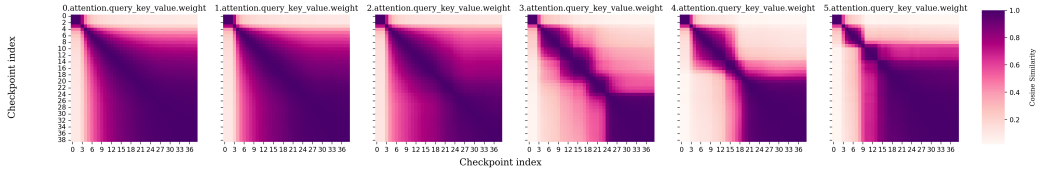

(b) query-key-value, weight

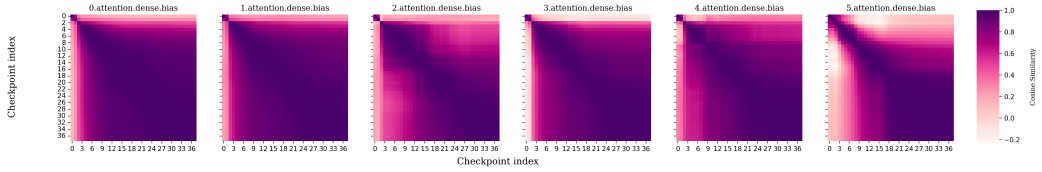

(c) dense, bias

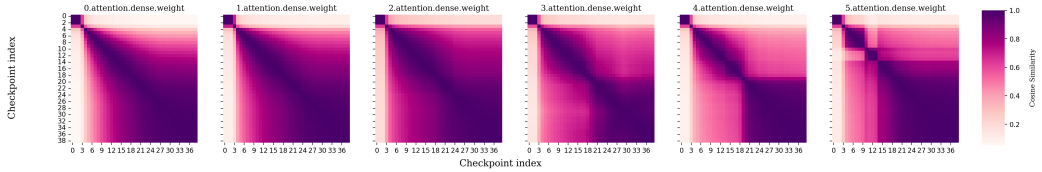

(d) dense, weight

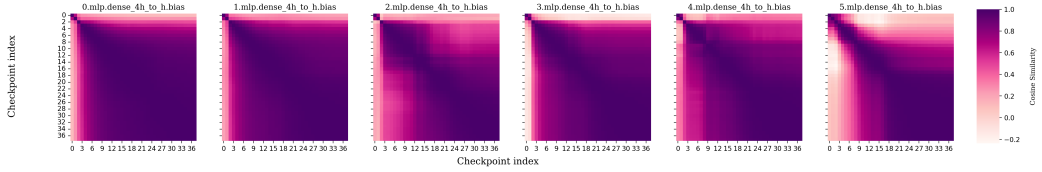

(e) dense-4h-to-h, bias

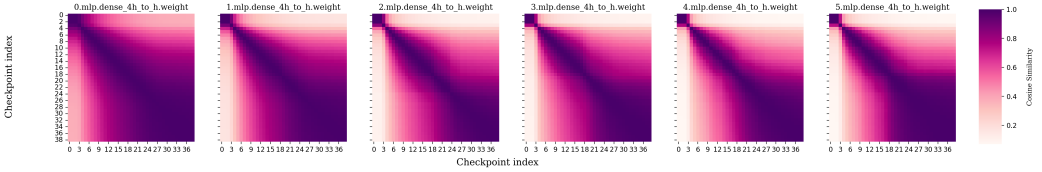

(f) dense-4h-to-h, weight

Figure 69. Layerwise Trajectory Maps, grouped by layer type, for the $14M$ GPT-NeoX model trained on the Pile dataset.

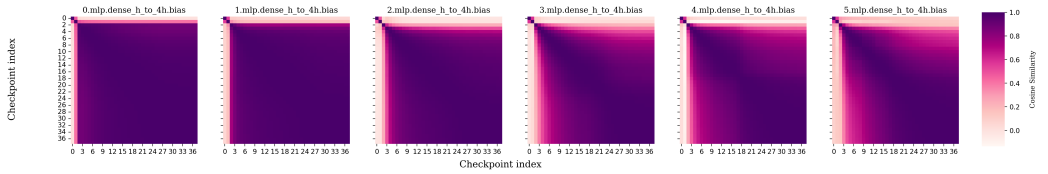

(a) dense-h-to-4h, bias

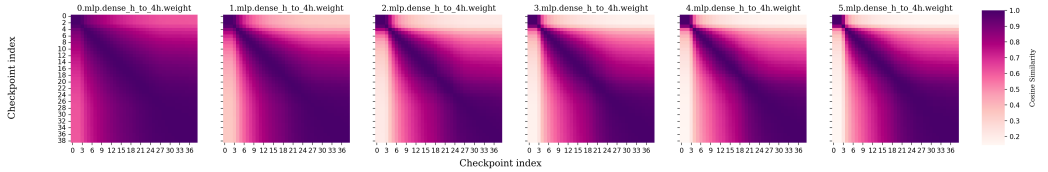

(b) dense-h-to-4h, weight

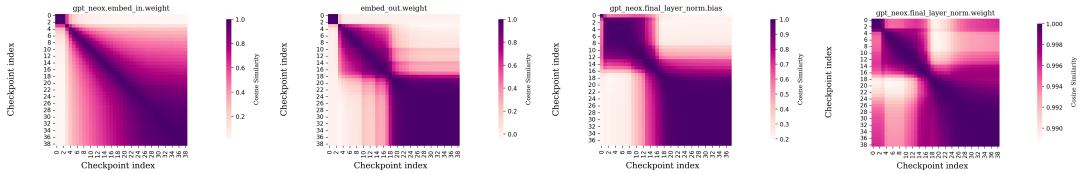

(c) embed-in, weight (d) embed-out, weight (e) final-layer-norm, bias (f) final-layer-norm, weight

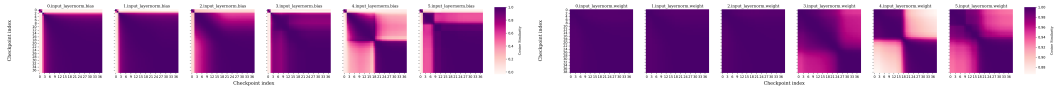

(g) input-layernorm, bias (h) input-layernorm, weight

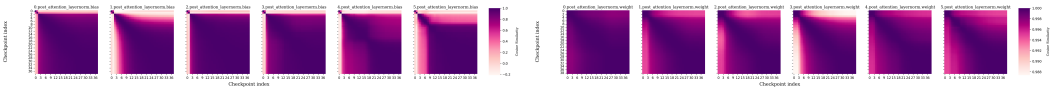

(i) post-attention-layernorm, bias (j) post-attention-layernorm, weight

Figure 70. Layerwise Trajectory Maps, grouped by layer type, for the $14M$ GPT-NeoX model trained on the Pile dataset.